A NUCLEAR $\mathcal{T}$-VIOLATION SEARCH USING OCTUPOLE-DEFORMED NUCLEI IN A CRYSTAL: PROPOSAL AND PROGRESS

by

Harish D. Ramachandran

A thesis submitted in conformity with the requirements
for the degree of Master of Science
Department of Physics
University of Toronto

A nuclear $\mathcal{T}$-violation search using octupole-deformed nuclei in a crystal: proposal and progress

Harish D. Ramachandran
Master of Science

Department of Physics
University of Toronto
2023

Abstract

New physics is required to solve a hitherto unsolved puzzle of our universe: the origin of the matter-antimatter asymmetry. At high energy scales, there must be new particles and interactions that violate time-reversal symmetry ($\mathcal{T}$). Existing constraints already place this new physics beyond the reach of direct detection via particle colliders, so experiments instead search for their effects via tiny $\mathcal{P}$-odd, $\mathcal{T}$-odd electromagnetic moments of fundamental particles within different composite systems. One conventional approach is to amplify these moments by measuring small energy shifts in *polarized* gas-phase atoms or molecules containing *deformed* nuclei.

In this report, I present a novel approach to search for $\mathcal{T}$-violating effects: an experiment that uses deformed nuclei within ions trapped in non-centrosymmetric sites in a macroscopic crystal. This solid-state approach is sensitive to new particles at the PeV scale in only a couple of days of integration time, owing to a much larger number of simultaneously addressable nuclei. This would present an improvement on experimental constraints by almost three orders of magnitude. I detail the techniques and measurement scheme that makes this approach viable and report on progress towards realizing this experiment with a crystal of ^{153}Eu^{3+}:Y$_2$SiO$_5$.

Acknowledgements

The last 15 months have been a wonderful time for me – both in physics and in life. I am grateful that I got to work every day on a project that I and others were so passionate about that it never felt like a job. When I decided to stick around for an MSc in April of last year, I could not have imagined it going any better in all facets than this. I have many people to thank for this amazing last year in Toronto.

First, I thank my advisor, Amar Vutha, for introducing me to precision measurements and growing my confidence and ability by giving me real responsibilities and creative freedom even when I was inexperienced. His wisdom and mentorship have been invaluable throughout the last four years.

On the ONIX experiment, I would like to specially thank (recent Master) Julia Ford, who greatly accelerated our progress to build a real, working experiment once they joined. Their energy and imagination made ONIX fun even when things weren't working, and inspired me to do things better all around. I want to thank undergrads Daniel Stedman and Alek Radak for entertaining commentary and excitedly approaching the problems we did not want to deal with and then actually solving them. I appreciate insightful discussions with Samuel Li, Mohit Verma, Andrew Jayich, and Mingyu Fan at various stages of the project. I also acknowledge funding from an NSERC Canada Graduate Scholarship.

I would like to thank my colleagues – Kristen Cote, Takahiro Tow, Dr. Scott Smale, and Dr. Shira Jackson – for answering obscure questions, run club on (some) Tuesdays, and much-needed coffee walks. They made the lab a welcoming, collaborative, and lively environment from the very start.

Finally, I would like to thank my friends and family for keeping me tethered to real life and reminding me to unwind. I would like to specially mention my friends and former roommates Aman Bhargava and Fred Chun; Kyup Lee; and my sister, Shayana.

Contributions

Research done during this MSc contributed to the works listed below. This report reproduces some material from these works.

Ref. [1]: **H. D. Ramachandran** and A. C. Vutha, Nuclear T-violation search using octupolar nuclei in a crystal, in *The 27th International Conference on Atomic Physics*, Jul 17 – 22, 2022, Royal Conservatory of Music, Toronto.

Ref. [2]: **H. D. Ramachandran** and A. C. Vutha, Nuclear T-violation search using octupole-deformed nuclei in a crystal, Phys. Rev. A **108**, 012819 (2023).

Ref. [3]: S. J. Li, **H. D. Ramachandran**, R. Anderson, and A. C. Vutha. Optical control of BaF molecules trapped in neon ice, New J. Phys **25**, 082001 (2023).

Ref. [4]: **H. D. Ramachandran**, J. E. Ford, and A. C. Vutha, Coherent quantum beats: spectroscopy of energy differences masked by inhomogeneous broadening, submitted to Phys. Rev. A, (2023), arXiv:2304.06189 [physics.atom-ph].

Contents

List of Tables

List of Figures

Chapter 1

Motivation

Fundamental physics research, in the modern era, is limited by a dearth of the experimental data required to formulate realistic theories beyond the Standard Model (BSM). There has yet to be any experimental observations at the 5σ level or higher that disagrees with the Standard Model. Yet the Standard Model is evidently not complete, as it leaves certain problems unsolved. One such mystery is the observed excess of matter over antimatter in the universe, unexplained by both the Standard Model and general relativity.

In order to produce a matter-dominant universe from an initial matter-antimatter balance, Andrei Sakharov showed that charge conjugation parity symmetry ($\mathcal{CP}$) violation – or, equivalently, time-reversal symmetry ($\mathcal{T}$) violation if we assume that $\mathcal{CPT}$ symmetry holds – is required [5]. Although $\mathcal{CP}$ violation is allowed within the Standard Model – through quark mixing (CKM phases), neutrino mixing (PMNS phases), and the $\bar{\theta}$ term – the experimentally observed rates of those interactions so far are not sufficient to explain the observed level of matter-antimatter asymmetry [6, 7, 8, 9, 10]. Therefore, new sources of time-reversal symmetry violation are necessary to explain the observed excess of matter over antimatter in the universe [11]. Theories beyond the Standard Model, and existing experimental constraints, indicate that the energy scale for this new physics is inaccessible to both present-day particle colliders [11, 12] and likely those in the foreseeable future [13].

Experimental searches for $\mathcal{T}$-violation are underway in both the leptonic and hadronic sectors, through precision measurements on a variety of systems with different measurement schemes. These include more direct searches, involving ultracold neutrons or storage rings containing protons, and indirect searches, involving composite systems such as atoms and molecules which have potentially $\mathcal{T}$-violating constituents. While direct searches benefit from more accurate theoretical predictions, indirect searches can nonetheless place stringent constraints on fundamental $\mathcal{T}$-violating parameters because they can be "background-free". Atoms and molecules are promising platforms for $\mathcal{T}$-violation searches because they are – to extremely good approximation – purely electromagnetic objects and quantum electrodynamics alone does not violate $\mathcal{T}$. Further, the $\mathcal{T}$-violation that *is* known to exist *within* the Standard Model leads to observables in atoms and molecules that are orders of magnitude below current experimental sensitivity [14, 15, 16, 17]. Thus, for the foreseeable future, any non-zero measurements of $\mathcal{T}$-violating observables in atomic or molecular systems would be a clear sign of physics beyond the Standard Model.

In this report, I propose a new experimental search for $\mathcal{T}$-violation in the hadronic sector. New physics sources of $\mathcal{T}$-violation coupled to hadrons lead to $\mathcal{P}$-odd, $\mathcal{T}$-odd nuclear moments – such as electric dipole moments (EDMs) and magnetic quaddrupole moments (MQMs) – which lead to measurable shifts in the energy levels of atoms [18]. I argue that a solid-state atomic $\mathcal{T}$-violation search with deformed nuclei offers the opportunity for a generational leap in sensitivity: a three order of magnitude improvement on experimental constraints on the QCD $\bar{\theta}$ term in only one day of integration time.

1.1 Deformed nuclei

On the face of it, a search for $\mathcal{P}$-odd, $\mathcal{T}$-odd nuclear moments using neutral atoms or molecules may appear futile due to screening effects. Within a neutral system, a nucleus with an EDM would polarize the electron cloud surrounding it, leading to an atomic EDM that exactly cancels out the nuclear EDM [19]. This "Schiff screening" effect is significant, but it leads to perfect cancellations only for point nuclei and non-relativistic electrons within neutral systems.

In particular, higher order electromagnetic moments of a *finite-sized* nucleus, such as the nuclear Schiff moment (NSM) and electric octupole moment, can lead to observable effects despite Schiff screening [20]. The NSM is an effective charge distribution on the surface of the nucleus, leading to a $\mathcal{T}$-violation-induced electric field $\vec{\mathcal{E}}_{\text{eff.}}$ inside the nucleus and parallel to the nuclear spin $\vec{I}$ [14]. Electrons penetrating the nucleus interact with $\vec{\mathcal{E}}_{\text{eff.}}$, leading to a $\mathcal{P}$-odd, $\mathcal{T}$-odd atomic EDM that produces measurable energy shifts in the atom or molecule. Nuclear MQMs, oscillating moments [14], and charged systems [20] also experience imperfect screening, leading to measurable energy shifts.

Symmetry-breaking nuclear moments (e.g., NSMs, MQMs) can be enhanced by up to three orders of magnitude in nuclei that exhibit a combination of quadrupole and octupole deformations [21, 22]. These deformations also reduce the difficulty (and thus uncertainties) of nuclear structure calculations relating NSMs or NQMs to fundamental $\mathcal{T}$-violating parameters [14]. For this reason, although the best existing atomic or molecular constraints on nuclear $\mathcal{T}$-violation come from the spherical ^{199}Hg nucleus [10], next-generation experiments typically involve deformed nuclei. Unfortunately, the majority of heavy, octupole-deformed nuclei – such as ^{223}Fr, ^{225}Ra, and ^{229}Pa – are also radioactive, adding severe experimental complexities.

1.2 Polarized atom and molecule experiments

The energy shifts induced in atoms by these $\mathcal{P}$-odd, $\mathcal{T}$-odd nuclear moments are magnified in atoms that are electrically polarized. Therefore $\mathcal{T}$-violating energy shifts can be greatly enhanced for deformed nuclei within polar molecules, wherein the constituent atomic ions are strongly polarized: this property has led to a number of experiments and proposals to study nuclear $\mathcal{T}$-violation using polar molecules [23, 24, 25, 26, 27].

To obtain competitive $\mathcal{T}$-violation sensitivities with polar molecules, it is typically necessary to cool and/or trap them so that they can be interrogated coherently for ≥ 1 s. An ultracold gas or beam of polar molecules can be prepared by e.g. direct laser cooling [26], molecular ion trapping [28], or ultracold polar molecule assembly [29]. Each technique presents its own unique challenges and compromises. Direct laser cooling must contend with the complex rovibrational structures of molecules, demanding many repumping lasers to keep molecules in the cooling cycle. Molecular ion traps can only hold a handful of ions, limiting spectroscopy precision unless extraordinary coherence times are reached (~ 1000 s would be necessary to improve existing $\bar{\theta}$ constraints by one order of magnitude in a couple of days of integration [30]). In most cases, the particular polar molecules containing deformed nuclei that are targeted by these experiments are both radioactive and (often, as a consequence) largely unstudied. This means a large body of work (e.g. laser spectroscopy) must be done before the $\mathcal{T}$-violation experiment can begin in earnest.

1.3 Solid-state challenges and opportunities

Fortunately, polar molecules are not the only way to polarize atoms. Atomic ions in non-centrosymmetric sites in a crystal are also strongly electrically polarized. In effect, each ion in such a crystal can be considered as being part of a very large polar molecule. Therefore experiments with nuclei enclosed by polarized ions can avail of enhanced internal electric fields, just as in polar molecule experiments, while also gaining sensitivity due to the enormous quantity of trapped ions that can be interrogated in cryogenically-cooled solid-state samples. The potential of experiments with such doped solids has been previously suggested by Singh [31] and Flambaum *et al.* [32].

However, there are two main challenges that need to be addressed before a $\mathcal{T}$-violation search experiment in a solid can be practically realized.

i) Although the ions in non-centrosymmetric sites are electrically polarized, the *average* electrical polarization over the crystal can still be zero: in other words, the electrical polarization vectors of ions within the crystal can point in many possible directions. Therefore, experiments on the full ensemble of ions in the crystal cannot measure $\mathcal{T}$-violating energy shifts, unless there is either a biased distribution of polarization vectors (e.g., in a ferroelectric crystal), or some way to separately measure signals from differently polarized ions.

ii) Optical and nuclear spin transitions of ions in solids undergo decoherence and inhomogeneous broadening in the solid-state, due to impurities, defects, phonons and the crystal fields from neighboring ions. Therefore, the techniques used for high signal-to-noise ratio measurements in gas-phase experiments, such as optical pumping and optically-detected magnetic resonance [10, 26], cannot be trivially ported over to solid-state experiments.

Thus, new measurement schemes are required in order to make practical advances in new physics searches in solids. These measurement schemes must also provide protection from systematic errors so that the high statistical sensitivity of solid-state systems can be gainfully exploited. In this report, I discuss the details of a measurement scheme that addresses both these challenges, expanding on the ideas presented in Refs. [1, 2]. I focus this discussion on the Eu:YSO system: $^{153}\mathrm{Eu}^{3+}$ ions doped into yttrium orthosilicate ($\mathrm{Y_2SiO_5}$), although the methods described here are more general and could be applied to other combinations of dopants and hosts. I also report on experimental progress towards a $\mathcal{T}$-violation search in Eu:YSO.

$^{153}\mathrm{Eu}$ is a stable isotope (52% natural abundance), and its collective enhancement of $\mathcal{T}$-violation effects is estimated to be comparable to those of $^{225}\mathrm{Ra}$ and $^{223}\mathrm{Fr}$ because of quadrupole and octupole deformations [32, 33]. Eu:YSO combines a number of advantages into one convenient platform: the intrinsic high sensitivity of $^{153}\mathrm{Eu}$ to nuclear $\mathcal{T}$-violation, large numbers of strongly polarized atomic ions, and well-studied hyperfine structure that enables high-precision measurements on its nuclear spin states. In Chapter 2, I describe the experimental measurement scheme and show how to use the properties of Eu:YSO to address challenges (i) and (ii). In Chapter 3, I describe progress towards an experimental apparatus to realize this measurement scheme in Eu:YSO. In Chapter 4, I describe our initial demonstrations of techniques involved in the measurement scheme. Finally, in Chapter 5, I summarize and lay out the next steps before the $\mathcal{T}$-violation measurement can be fully realized.

Chapter 2

Scheme

In this chapter, I explain in detail why Eu:YSO paired with a new measurement scheme we have devised gives rise to an extremely high sensitivity $\mathcal{T}$-violation experiment. First, I describe the Eu:YSO system, which has been studied in detail in previous works, and highlight why its properties are conducive to the experiment. I then describe a novel measurement scheme that utilizes these properties. Finally, I estimate the sensitivity of the proposed experiment to fundamental $\mathcal{T}$-violating parameters. This chapter contains material from Refs. [1, 2, 4], as listed on page iv.

2.1 Structure of Eu:YSO

YSO is a transparent crystal where the Y^{3+} ions are located in non-centrosymmetric sites. Eu^{3+} ions substitute for Y^{3+} at two distinct C_1 sites: one with 7 adjacent oxygen ions ("site 1") and the other with 6 adjacent oxygen ions ("site 2") [34]. Eu:YSO has been extensively studied over several decades, primarily for its applications to quantum information storage and transduction [35, 36, 37]. In particular, narrow homogeneous and inhomogeneous linewidths have been observed on the $4f^6\,{}^7F_0 \to 4f^6\,{}^5D_0$ transition at 580 nm [38]. The hyperfine and Zeeman interactions of the nuclear sublevels in the ${}^7F_0$ and ${}^5D_0$ electronic states have been measured [39], optical pumping between the nuclear sublevels has been demonstrated [40], and long-lived coherence between these sublevels has been observed [41]. We focus the subsequent discussion on ions in substitution site 1, as their electronic and hyperfine properties in the ${}^7F_0$ and ${}^5D_0$ states have been studied in more detail.

Notably, linear Stark shifts of the ${}^7F_0 \to {}^5D_0$ transition have been observed in Eu:YSO [42]. A linear Stark shift implies that Eu^{3+} ions are statically polarized within the crystal. Static electric polarization of ions is not unusual – in fact, this is what happens to the cations and anions in a polar molecule. But the difference between a gas-phase polar molecule and Eu:YSO is that gas-phase molecules exist in a quantum superposition of states with different orientations of their body-fixed dipole (i.e., rotational states), whereas Eu^{3+} ions in Eu:YSO are projected into a classical statistical mixture of fixed orientations due to suppression of tunneling by the lattice. Eu:YSO therefore consists of a set of electrically polarized Eu^{3+} ions, fixed in their orientation by the YSO crystal.

Despite being strongly electrically polarized and bonded to a set of neighboring O^- ions as if in a polar molecule, Eu^{3+} ions have an unusual property which is crucial to the measurement scheme described in Section 2.2: the lowest few electronic states in the ion retain their atom-like character. This property arises because the valence energy levels in Eu^{3+}, particularly the ${}^7F_0$ and ${}^5D_0$ states that are involved in the 580 nm optical transition, lie within the contracted and shielded f-shell [43, 42]. Furthermore, these states have zero electronic angular momenta, which drastically reduces their coupling to the lattice. The Eu:YSO system

thus offers the combined benefits of atom-like narrow optical lines along with polar-molecule-like enhancement of $\mathcal{T}$-violation effects.

We parameterize the polarization of an Eu^{3+} ion by its induced dipole moment $D\hat{n}$. In *non-centrosymmetric* sites, an electronic state of the ion can have a finite electric dipole moment D due to odd-parity crystal field components and can thus exhibit linear Stark shifts [44]. This effect leads to symmetric doublet splittings in optical transitions when two states with oppositely-oriented dipole moments (relative to the crystallographic axes) are degenerate in a non-centrosymmetric trapping site – following the first observations in ruby crystals, this mechanism was named "pseudo-Stark splitting" (PSS) [45]. Similar to the description of Ref. [46], in the case of the non-centrosymmetric C_1 trapping sites of YSO, the orientation of the dipole moment is fixed in an arbitrary direction relative to the crystallographic axes. However, within the overall *centrosymmetric* YSO lattice ($C2/c$), the dipole moment is oriented relative to a pair of equivalent crystallographic directions, leading to Eu^{3+} ions with oppositely-oriented dipole moments in otherwise-physically-equivalent trapping sites in the macroscopic crystal.

The shift of the 580 nm transition in Eu:YSO in a lab electric field, $\vec{\mathcal{E}}_{\text{lab}}$, is $\Delta E = -\Delta D\hat{n} \cdot \vec{\mathcal{E}}_{\text{lab}}$, where $\Delta D = D(^7F_0) - D(^5D_0)$ is the differential dipole moment between the $^7F_0$ and $^5D_0$ electronic states. In the linear Stark shift measurements of Ref. [42], an optically selected spectral class of ions prepared in $\mathcal{E}_{\text{lab}} = 0$ split into two classes shifted by opposite amounts when $\mathcal{E}_{\text{lab}} \neq 0$ was applied. These measurements are consistent with the prior argument: that each unit cell in Eu:YSO has a static electric dipole moment $D\hat{n}$, and that the cells are found in two opposite orientations along each crystallographic axis in the macroscopic single crystal. The linear Stark shift coefficient $\Delta E = 27.1 \text{ kHz}/(\text{V/cm}) \times \mathcal{E}_{\text{lab}}$ of the $^7F_0 \to {}^5D_0$ transition measured in Ref. [42], for electric fields directed along the crystallographic D_1 axis, indicates that the differential dipole moment along the D_1 axis is $\Delta D = 0.02 \, ea_0$. As described below, the linear Stark shift of the optical transition provides a way to selectively address ions that have a specific direction of electric polarization $\hat{n}$.

The effective Hamiltonian for the nuclear spin degrees of freedom, which accurately describes the hyperfine structure of $^{153}Eu^{3+}$ in YSO, is

$$\hat{H}_{\text{eff}} = \vec{\mathcal{B}}_{\text{lab}} \cdot \mathbf{M} \cdot \vec{I} + \vec{I} \cdot \mathbf{Q} \cdot \vec{I} - D\hat{n} \cdot \vec{\mathcal{E}}_{\text{lab}} + W_T \vec{I} \cdot \hat{n}. \tag{2.1}$$

Here $\vec{I}$ is the nuclear spin, $\vec{\mathcal{E}}_{\text{lab}}$ is the lab electric field, and $\vec{\mathcal{B}}_{\text{lab}}$ is the lab magnetic field. $\mathbf{M}$ is the gyromagnetic tensor [47], such that $\vec{\mu} = \mathbf{M} \cdot \vec{I}$ is the magnetic moment. $\mathbf{Q}$ is the quadrupole tensor, and $D\hat{n}$ is the electric dipole moment of the Eu^{3+} ion polarized by the crystal. The quantity W_T parameterizes the nuclear $\mathcal{T}$-violating energy shift. Since $\mathbf{M}$ and $\mathbf{Q}$ are influenced by crystal fields, they depend on the electronic state ($^7F_0$ or $^5D_0$), and they are anisotropic for the C_1 substitution sites where the $^{153}Eu^{3+}$ ions are trapped in Eu:YSO. The $\mathbf{M}$ tensor has been measured for ^{151}Eu:YSO [48], but not for the ^{153}Eu isotope that is of interest here. Therefore, as a reasonable first approximation, we scaled the $\mathbf{M}$ tensor in Ref. [48] by the ratio of the nuclear magnetic moments of ^{153}Eu to ^{151}Eu [49] for our calculations.

The eigenstates of this Hamiltonian for the $^7F_0$ electronic state in the absence of external fields (and with $W_T = 0$) are represented as points in the diagram in Fig. 2.1. The eigenstates appear in degenerate pairs that are related to each other by a $\mathcal{T}$-transformation, as expected from Kramers' degeneracy theorem for half-integer spin systems [50]. We denote these Kramers pairs as $\bar{a}, a, \bar{b}, b$ and $\bar{c}, c$ in increasing order of energy. We use this nomenclature for the eigenstates instead of m_I labels that appear in the literature, since m_I is not a good (or particularly useful) quantum number when there is no azimuthal symmetry. Also shown in Fig. 2.1 are the sensitivity coefficients $\zeta = \left\langle \vec{I} \cdot \hat{n} \right\rangle$ in each state — these values are proportional to the energy shift of the state if $\mathcal{T}$-violation were present. $\mathcal{T}$-violating energy shifts have equal magnitude and opposite sign for the two states in a Kramers pair. So in a nutshell, the experiment involves searching for the

breakdown of Kramers' degeneracy due to $\mathcal{T}$-violation.

Note, however, that the states in a Kramers pair have opposite signs of magnetic moments as well. Therefore, the experiment needs to be able to distinguish $\mathcal{T}$-violating energy shifts from mundane Zeeman shifts due to magnetic fields. This is easily accomplished: the ζ values for any given state have equal magnitude, but *opposite signs*, in ions with opposite values of $\hat{n}$ (i.e., ions with opposite electric polarization). So the experiment consists of measuring energy differences between a Kramers pair in ions that are polarized in a particular direction in the lattice, and comparing the result with the same measurement in ions polarized in the opposite direction. For definiteness, the measurement scheme in Section 2.2 focuses on measuring the $\mathcal{T}$-violating energy difference between the states labelled as $|\bar{a}\rangle$ and $|a\rangle$ in Fig. 2.1.
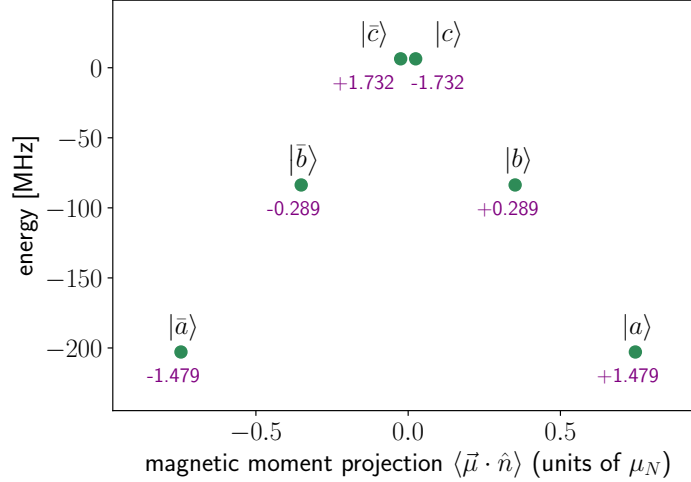

Figure 2.1: Energies, magnetic moment projections $\langle \vec{\mu} \cdot \hat{n} \rangle$, and nuclear $\mathcal{T}$-violation sensitivity parameters $\zeta = \left\langle \vec{I} \cdot \hat{n} \right\rangle$ (purple text) for nuclear spin sublevels of the $^7F_0$ electronic state of $^{153}Eu^{3+}$ in YSO in zero magnetic field. These values were calculated using the constants measured in Refs. [51, 48], adjusted as described in the text. We fixed $\hat{n}$ parallel to the crystallographic D_1 axis of YSO for this calculation.

A key step in the measurement scheme is the transfer of population into specific Kramers pairs through optical pumping. Note that, at any given optical frequency within the inhomogeneous optical line, ions from many different spectral classes (i.e., local crystal environments) can be resonant with the laser. Each spectral class is associated with nine distinct optical frequencies, from the combinations of three Kramers pairs each in $^7F_0$ and $^5D_0$.

	$|a\rangle$	$|\bar{a}\rangle$	$|b\rangle$	$|\bar{b}\rangle$	$|c\rangle$	$|\bar{c}\rangle$
$\langle a_e|$	0.031	0.001	0.157	0.012	0.799	0.000
$\langle \bar{a}_e|$	0.001	0.031	0.012	0.157	0.000	0.799
$\langle b_e|$	0.094	0.004	0.690	0.026	0.163	0.022
$\langle \bar{b}_e|$	0.004	0.094	0.026	0.690	0.022	0.163
$\langle c_e|$	0.866	0.004	0.105	0.009	0.007	0.009
$\langle \bar{c}_e|$	0.004	0.866	0.009	0.105	0.009	0.007

Table 2.1: Relative transition probabilities $|\langle j_e|i\rangle|^2$ between hyperfine sublevels of $^7F_0 \rightarrow {}^5D_0$ in ^{153}Eu:YSO in zero magnetic field, calculated using the constants measured in Refs. [51, 52]. Hyperfine levels belonging to the excited electronic state are denoted with the subscript "e".

In contrast with gas-phase atoms, Eu:YSO can be optically pumped into selected hyperfine states despite the lack of electronic angular momentum in $^7F_0$ and $^5D_0$. The main reason is that the quadrupole tensor $\mathbf{Q}$ is different in the $^7F_0$ and $^5D_0$ states, and so the hyperfine eigenstates in these two electronic states have

different orientations of $\vec{I}$ relative to the crystallographic axes. Therefore, the absorption or spontaneous emission of a photon on the $^7F_0 - {}^5D_0$ transition can reorient $\vec{I}$, resulting in finite optical transition matrix elements between any $^7F_0$ hyperfine state $|i\rangle$ and $^5D_0$ hyperfine state $|j_e\rangle$. These optical transition matrix elements are listed in Table 2.1. Applying optical pulses with appropriate sidebands to address multiple states, it is possible to selectively populate the $\bar{b}, b$ Kramers pair in $^7F_0$.
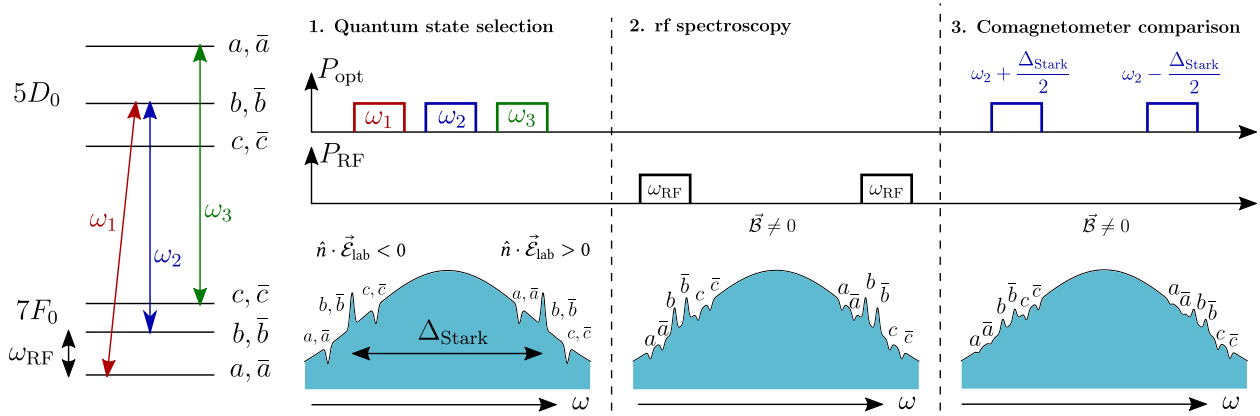
2.2   Measurement scheme

Figure 2.2: Overview of the measurement scheme. The $^7F_0 - {}^5D_0$ optical transition in Eu:YSO is used to optically pump the nuclear spin sublevels. In Step 1, laser sidebands tuned to different hyperfine transitions are used to deplete the $a, \bar{a}$ and $c, \bar{c}$ states – creating holes in the inhomogeneously broadened optical line – and to populate the $b, \bar{b}$ states, which creates antiholes [53]. Applying a lab electric field moves the holes and antiholes to different spectral neighborhoods as shown in the diagram, depending on the relative orientation between $\vec{\mathcal{E}}_{\text{lab}}$ and the dopant ion's electrical polarization $\hat{n}$. In Step 2, rf pulses are used to drive the $\bar{b} - \bar{a}$ and $b - a$ transitions. In Step 3 the populations excited into $a, \bar{a}$ are detected using optical absorption, and the rf resonance frequencies are compared for opposite orientations of $\hat{n}$. A similar method can be used for measuring the $\bar{b} - \bar{c}$ and $b - c$ transition.

The measurement sequence, illustrated in Fig. 2.2, is as follows.

1. **State selection.** The 580 nm $^7F_0 - {}^5D_0$ optical transition of Eu^{3+}, with appropriately chosen rf sidebands, is used to deplete the $|a\rangle, |\bar{a}\rangle$ and $|c\rangle, |\bar{c}\rangle$ states, and pump the population into $|b\rangle, |\bar{b}\rangle$.

2. **rf spectroscopy.** In order to precisely measure the $\mathcal{T}$-violating energy shift, the $\{b, \bar{b}\} \leftrightarrow \{a, \bar{a}\}$ transitions are driven using a sequence of rf pulses.

3. **Comagnetometer comparison.** Populations transferred to $a, \bar{a}$ by the rf pulses are detected using optical absorption, in order to measure the rf resonance frequencies. The resonances measured in this way are compared for ions with opposite values of $\hat{n}$, taking advantage of the Stark shifts of the optical transitions.

In Step 1, Eu^{3+} ions are initialized in the $\bar{b}, b$ states using a sequence of laser pulses. In gas-phase atoms, two lasers (one to deplete $\bar{a}, a$ and one to deplete $\bar{c}, c$) would be sufficient to transfer population to the $\bar{b}, b$ Kramers pair. But due to inhomogeneous broadening of the $^7F_0 - {}^5D_0$ optical transition in Eu:YSO, these two lasers also *depopulate* the desired $\bar{b}, b$ Kramers pair in spectral classes whose optical resonances are shifted by linear combinations of the $^7F_0$ and $^5D_0$ hyperfine intervals. Therefore three different optical frequencies are necessary to ensure that one spectral hole (or anti-hole) is uniquely associated with one Kramers pair. The illustration for Step 1 in Fig. 2.2 shows these laser frequencies. A detailed description of the hyperfine state-preparation protocol can be found in Section 4.4 and Ref. [40].

In Step 2, a small bias magnetic field $\mathcal{B}_{\text{lab}}$ is applied for experimental convenience, so that nonzero frequencies can be measured. rf spectroscopy of the $\{b, \bar{b}\} \leftrightarrow \{a, \bar{a}\}$ transitions is then used to measure the frequency difference between the $\bar{a}, a$ states, $\nu_{\bar{a}a}$. A nonzero value of $\nu_{\bar{a}a}$ arises due to the Zeeman shift from the bias field, plus a putative shift due to the presence of $\mathcal{T}$-violation.

The main obstacle to precision rf spectroscopy of $\nu_{\bar{a}a}$ is the inhomogeneous broadening of the $\{b, \bar{b}\} \leftrightarrow \{a, \bar{a}\}$ rf transitions. On the face of it, the precision of $\nu_{\bar{a}a}$ would seem to scale as $1/\sqrt{T_2^*}$ with the ensemble coherence time $T_2^* \sim 1/\Gamma_{\text{inh}}$ arising from the inhomogeneous width Γ_{inh} of the $\{b, \bar{b}\} \leftrightarrow \{a, \bar{a}\}$ transitions. Although Eu:YSO would nonetheless offer competitive $\mathcal{T}$-violation constraints with $T_2^* \sim 2.3 \, \mu$s [36], it is in fact possible to obtain much better precision, scaling inversely with the *hyperfine coherence time* $T_2 = 15$ ms [54, 55, 41].

The key to measuring the small frequency difference $\nu_{\bar{a}a}$, despite its being masked by inhomogeneous broadening, is to use coherent quantum beat (CQB) spectroscopy [4]. The CQB method is described in Section 2.4, and further details can be found in Ref. [4]. In Step 2, applying CQB to the four-level system – $b, \bar{b}$ and $a, \bar{a}$ – allows for simultaneous measurements of $\nu_{\bar{a}a}$ on the entire ensemble of Eu^{3+} nuclear spins prepared in Step 1, leading to larger signals and longer coherence time. Inhomogeneous broadening of the hyperfine transitions is not a fundamental barrier to precision measurements of $\mathcal{T}$-violation in solid-state systems.

In Step 3, we take advantage of the $^7F_0 - {}^5D_0$ transition to optically read out the populations in the $\bar{b}, b, \bar{a}, a$ states, using absorption or fluorescence spectroscopy. Crucially, these populations can be *separately* measured for Eu^{3+} ions polarized in opposite directions. Due to the linear Stark shift and the sub-kHz homogeneous linewidth of the $^7F_0 - {}^5D_0$ transition, a small lab electric field, $\mathcal{E}_{\text{lab}} \approx 5$ V/cm, suffices to widely separate the optical transitions in ions with opposite values of $\hat{n}$. These oppositely polarized ions then serve as ideal "co-magnetometers", with properties that are completely identical in every way except for the sign of the $\mathcal{T}$-violating energy shift.

2.2.1 Suppression of systematic errors

During the measurement, spectroscopy of the $\nu_{\bar{a}a}$ can be repeated while varying a number of experimental parameters. These parameters include, but are not limited to, the static magnetic and electric field strengths, rf pulse amplitudes and phases, the volume illuminated by the laser within the crystal, and the spectral class of Eu^{3+} ions that are optically state-selected. These variations can be augmented with a number of "reversals", i.e. discrete switches, of parameters such as the signs of the static electric and magnetic fields. The reversals modulate the energy shifts from a true $\mathcal{P}$-odd $\mathcal{T}$-odd nuclear moment (proportional to ζ) in a characteristic way, allowing us to separate $\mathcal{T}$-violation signals from spurious systematics.

A useful comparison for distinguishing true $\mathcal{T}$-violation in such measurements uses the "co-magnetometer" ions mentioned above. This process is analogous to the effect used to great advantage in electron EDM experiments with polar molecules [56]. Additionally, since the ion is already strongly polarized within the crystal, variations in the small applied electric field $\mathcal{E}_{\text{lab}}$ do not appreciably change the $\mathcal{T}$-violating energy shift. Thus the value of ζ is essentially unaffected by variations in the magnitude of $\mathcal{E}_{\text{lab}}$. On the other hand many classes of systematic errors, e.g. due to non-reversing electric fields or leakage currents caused by the fields, strongly depend on $\mathcal{E}_{\text{lab}}$. Therefore experiments conducted with different values of $\mathcal{E}_{\text{lab}}$ allow a large variety of systematic errors to be distinguished from genuine signals.

Yet another useful switch is to interleave measurements on the $\{b, \bar{b}\} \leftrightarrow \{a, \bar{a}\}$ transitions with measurements on other pairs such as $\{b, \bar{b}\} \leftrightarrow \{c, \bar{c}\}$ (see Fig. 2.1) under otherwise identical conditions. These comparisons, between sets of states with very different values of ζ and different magnetic moments, will affect a true $\mathcal{T}$-violation signal in a characteristic and calculable way, distinct from errors due to uncompensated

Systematic effect	Methods for detection and suppression
$\mathcal{B}$-field drifts	$\hat{n}$ switch, spin states switch, isotope switch
Non-reversing $\mathcal{B}$-fields	$\mathcal{E}_{\text{lab}}$ magnitude, $\hat{n}$ switch, spin states switch, isotope switch
Non-reversing $\mathcal{E}$-fields	$\mathcal{E}_{\text{lab}}$ magnitude, spin states switch, isotope switch
Laser light shifts	$\mathcal{E}_{\text{lab}}$ magnitude, $\hat{n}$ switch, spin states switch, isotope switch
rf light shifts/pulse errors	$\vec{\mathcal{B}}_{\text{lab}}$ reversal, $\hat{n}$ switch, isotope switch, rf pulse magnitude and width
Phonon effects	above switches plus crystal temperature variation
Crystal impurities/defects	differently doped or enriched crystals

Table 2.2: Potential systematics and paths to their suppression in the experiment. The technical simplicity of the experimental system, coupled with the many useful controls available in Eu:YSO, enables $\mathcal{T}$-violating energy shifts to be cleanly distinguished from mimicking systematics.

magnetic fields.

Finally, another convenient switch is offered by comparisons between measurements on $^{151}\text{Eu}^{3+}$ and $^{153}\text{Eu}^{3+}$ isotopes under otherwise identical measurement parameters. These ions have the same nuclear spin ($I = 5/2$), nearly equal natural isotopic abundance and comparable atomic and magnetic moments, but only ^{153}Eu has the nuclear octupole deformation which enhances the effects of microscopic $\mathcal{T}$-violation [33]. Therefore the two isotopes offer one more useful co-magnetometer-like comparison. Using the shift in the hyperfine Hamiltonian between these isotopes, a simple change in the laser frequencies used in Step 1 above allows switching between the isotopes within the same crystal, in order to separate $\mathcal{T}$-violation signals from systematics.

Table 2.2 summarizes some of the systematic error controls available with this combination of experimental platform and measurement scheme.

The Eu:YSO system has a number of practical advantages for experiments. The crystal occupies a small volume, making it conveniently easy to shield from background electromagnetic fields. It is simple to operate experiments with multiple crystals (e.g., with different doping concentration, or different isotopic enhancements) within the measurement volume or to change the temperature of the crystal. A single laser, with appropriate rf sidebands imprinted by acousto- or electro-optic modulators, is adequate for the state-preparation and readout steps. The crucial spectroscopy step is done entirely using rf spectroscopy, which allows for precise control of the pulse amplitudes and phases.

2.3   Estimated sensitivity to new physics

The essence of the experiment is to search for a $\mathcal{T}$-violating energy shift between different orientations of the ^{153}Eu nucleus within a polarized Eu^{3+} ion. The sensitivity of this process to $\mathcal{T}$-violation is determined by (i) the polarization of the Eu^{3+} ion by the crystal, which results in $\mathcal{T}$-violating energy shifts, (ii) the intrinsic sensitivity of the ^{153}Eu nucleus to fundamental $\mathcal{T}$-violation parameters, and (iii) the statistical precision with which the $\mathcal{T}$-violating shift is measured.

In the following, we will estimate the polarization of the Eu^{3+} ions in Eu:YSO using published experimental measurements and theory calculations. First, we introduce a quantity that we denote as the crystal electric field, $\vec{\mathcal{E}}_{\text{xtl}}$. This is the field that one would have to apply to a free-space ion to obtain the induced dipole moment $D\hat{n}$ of the Eu^{3+} ions in Eu:YSO. The magnitude of $\mathcal{E}_{\text{xtl}}$ can be estimated from the measured linear Stark shift of the $^{7}F_0 - {}^{5}D_0$ transition.

The linear shift measured in experiments arises from an underlying quadratic shift that involves the crystal electric field and the atomic polarizabilities: $\Delta E = \Delta\alpha \left(\vec{\mathcal{E}}_{\text{xtl}} + \vec{\mathcal{E}}'_{\text{lab}} \right)^2$, where $\mathcal{E}'_{\text{lab}} = \mathcal{E}_{\text{lab}}/\epsilon_r$ is the lab field shielded by the permittivity $\epsilon_r \approx 10$ [57] of the crystal. The atomic polarizability difference between the $^{5}D_0$ and $^{7}F_0$ states is $\Delta\alpha = \alpha_e - \alpha_g$. Therefore $\Delta\nu_E = 2\Delta\alpha \, \vec{\mathcal{E}}_{\text{xtl}} \cdot \vec{\mathcal{E}}'_{\text{lab}}$.

In order to estimate $\mathcal{E}_{\text{xtl}}$ from the measured Stark shift coefficient $\Delta\nu_E \sim 27$ kHz/(V/cm) [42], we need estimates of $\Delta\alpha$. The differential polarizability of the states in Eu:YSO is presently unknown, although the polarizability of the ground state of the ion is known to be $\alpha_g = 1.1$ a.u. in free space [58]. In order to conservatively account for the higher polarizability of the ion within the YSO lattice [59], and for the unknown (although likely much smaller [59]) polarizability of the $^5D_0$ state, we assume in the worst-case that $\Delta\alpha = 100$ atomic units. The resulting estimate of the crystal electric field is $\mathcal{E}_{\text{xtl}} \gtrsim 1.3$ MV/cm.

Next, the $\mathcal{T}$-violating energy shift measured in experiments can be related to a microscopic measure of $\mathcal{T}$-violation. We write the $\mathcal{T}$-violating shift discussed in Section 2.2 as $\nu_{\bar{a}a} = 2\zeta_a\,\kappa\,\theta\,\mathcal{E}_{\text{xtl}}$, where ζ_a is the absolute value of the ζ parameter in the $\bar{a}, a$ states. The quantity θ is the equivalent value of the quantum chromodynamics $\bar{\theta}_{\text{QCD}}$ parameter that would lead to the same physical effects, and is thus a convenient dimensionless way to quantify $\mathcal{T}$-violation due to new physics. The value of κ has been calculated for $^{153}\text{Eu}^{3+}$ in Ref. [32] to be $\kappa(^{153}\text{Eu}) = -1.2 \times 10^{-17}$ e cm. Thus we arrive at an estimate of the $\mathcal{T}$-violating shift in Eu:YSO, which is $\nu_{\bar{a}a} \sim 1.1 \times 10^4\,\theta$ Hz. Alternatively, we can parameterize the $\mathcal{T}$-violating shift $\nu_{\bar{a}a} = 2\zeta_a\,\xi\,\eta\,\mathcal{E}_{\text{xtl}}$ in terms of the strength of the new physics interactions it constrains, which is expected to scale as $\eta \sim \left(\frac{v}{f}\right)^2$ on dimensional grounds [17, 60]. Here f is the new physics energy scale and $v \sim 200$ GeV is the electroweak scale. With $\xi(^{153}\text{Eu}) = -3.6 \times 10^{-23}$ e cm calculated in Refs. [32, 33], we arrive at $\nu_{\bar{a}a} \sim 3.3 \times 10^{-2}\,\eta$ Hz.

The above numbers are based on a highly conservative estimate of $\mathcal{E}_{\text{xtl}}$. More accurate estimates of the new physics and dark matter sensitivities of the Eu:YSO system will need to be supported by accurate calculations of the electrical polarization of Eu^{3+} in non-centrosymmetric sites [1].

The experimental precision in measuring the $\mathcal{T}$-violating shift depends on three factors: the number of Eu^{3+} ions involved in a measurement, N, the nuclear spin coherence time, T_2, and the total integration time, T_{int}. Assuming an Eu concentration of 0.01%, a 1-mm-diameter laser beam propagating through a 10-mm-long crystal, and optical state-selection over a 100-kHz linewidth, we estimate the number of ions resonant with the laser to be $N = 10^{14}$. As mentioned above and further discuss in Section 2.4, coherent quantum beat spectroscopy allows measurements of $\nu_{\bar{a}a}$ with a coherence time that is not limited by the ensemble T_2^* for nuclear spin transitions. For the estimate of new physics sensitivity, we use $T_2 = 15$ ms measured at 4 K in Refs. [54, 55, 41].

The precision in the measurement of the $\mathcal{T}$-violating shift is

$$\delta\nu = \frac{1}{2\mathcal{S}}\sqrt{\frac{1+\beta}{T_2 T_{\text{int}}}} \tag{2.2}$$

where $\mathcal{S}$ is the signal-to-noise ratio of population measurements that can be obtained within a measurement time $T_m = \beta T_2$. Here $1 + \beta$ is a duty-cycle factor that encapsulates how efficiently the measurements use the available coherence time. We assume that the full extent of the signal-to-noise from $N = 10^{14}$ ions, $\mathcal{S} = 10^7$, can be obtained in a measurement time $T_m = 2T_2$ (i.e., $\beta = 2$), using low-noise laser absorption measurements of the hyperfine state populations. These estimates suggest a statistical sensitivity $\delta\nu \sim 2.4$ nHz $\times \sqrt{\frac{1\,\text{day}}{T_{\text{int}}}}$.

Combining the estimate of $\mathcal{T}$-violating shift in the Eu:YSO system, $\nu_{\bar{a}a}$, with the precision obtainable from the measurement scheme, $\delta\nu$, we find that the resulting $\mathcal{T}$-violation sensitivity is $\delta\theta \lesssim 2.2 \times 10^{-13}\sqrt{\frac{1\,\text{day}}{T_{\text{int}}}}$ or $\delta\eta \lesssim 7.3 \times 10^{-8}\sqrt{\frac{1\,\text{day}}{T_{\text{int}}}}$. The realization of the scheme developed in this paper could lead to a considerable improvement over current bounds e.g. $\delta\bar{\theta}_{\text{QCD}} < 2 \times 10^{-10}$ on $\mathcal{T}$-violation [62, 10, 17], probing new physics interactions at energy scales $\gtrsim 1$ PeV in only two days of integration time.

We note that nuclear spin coherence for thousands of seconds has been demonstrated in the Eu:YSO system at high magnetic fields [48, 35]. While we have conservatively made our estimate using the much

---

[1]A calculation for a similar system, EuCl_3, has been presented in Ref. [61].

smaller value of T_2 in low magnetic fields reported for Eu:YSO in the literature, it is enticing to anticipate new measurement techniques that could potentially unlock much longer coherence times for $\mathcal{T}$-violation measurements in Eu:YSO.

In addition to $\mathcal{P}$-odd, $\mathcal{T}$-odd nuclear moments, $\mathcal{T}$-violation can also appear due to time-dependent phenomena, such as oscillating electric dipole moments arising from wave-like dark matter [63, 64, 65]. Any such oscillations need to be measured with a bandwidth higher than two inverse periods, else they average away to zero. The high sensitivity obtainable within a short integration time using Eu:YSO leads to useful bandwidth: we expect to be sensitive to fluctuations $\delta\theta < 10^{-10}$ within one second of integration, enabling a broadband search for wave-like dark matter over the mass range from $10^{-14} - 10^{-18}$ eV.

2.4   Coherent quantum beats

In this section, we describe the method of coherent quantum beat (CQB) spectroscopy that enables the measurement of small energy differences buried within inhomogeneous broadening, without relying on spontaneous emission. The CQB technique is applied in step 2 of our measurement scheme, described in Section 2.2, so we highlight its important features here. Further details can be found in Ref. [4].

2.4.1   Details of the technique

Consider the following problem in precision spectroscopy: an experimenter wants to measure a small energy difference ω_e between a pair of nearly-degenerate levels $|e_1\rangle$ and $|e_2\rangle$. Directly driving the transition between $e_1 \rightarrow e_2$ happens to be impractical due to the smallness of ω_e, and so ω_e is measured by driving transitions between $|e_1\rangle, |e_2\rangle$ and a third state $|g\rangle$. In such a scheme, the broadening of the $g \rightarrow e_i$ transitions limits the precision of the ω_e measurement. A well-known method for circumventing inhomogeneous broadening is quantum beat spectroscopy [66, 67, 68], which has a long history of applications (see, e.g., [69, 70, 71, 72, 73] among others). However, quantum beat spectroscopy relies on spontaneous emission, which precludes its use in precision measurements of long-lived electronic states, hyperfine states or spin sublevels.
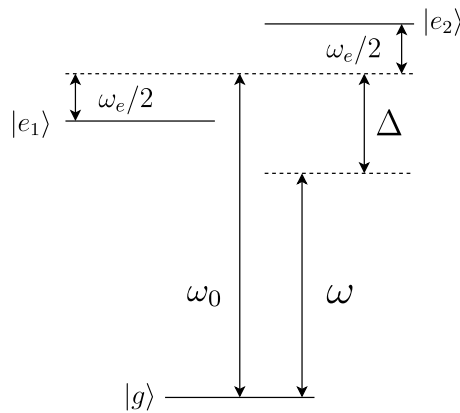

Figure 2.3: A system of three levels, where the energy difference of interest (ω_e) is measured using spectroscopy of the $g \rightarrow e_1$ and $g \rightarrow e_2$ transitions. The frequency of light is ω and the average of the $g \rightarrow e_1, e_2$ resonance frequencies is ω_0. The driving frequency is detuned from the resonant frequency by Δ.

Let the ensemble of atoms participating in the measurement be initially in the state $|g\rangle$ and consider atoms that interact with light that has frequency ω, as shown in the energy level diagram in Fig. 2.3. We denote the average of the $g \rightarrow e_1, e_2$ resonance frequencies as ω_0, and define the detuning $\Delta = \omega - \omega_0$.

We assume that the Rabi frequency is identical for the $g \to e_i$ ($i = 1, 2$) transitions, defining it to be $\Omega = \frac{1}{\sqrt{2}} \langle e_1 | H_{\text{int}} | g \rangle = \frac{1}{\sqrt{2}} \langle e_2 | H_{\text{int}} | g \rangle$, where H_{int} is the atom-field interaction Hamiltonian.
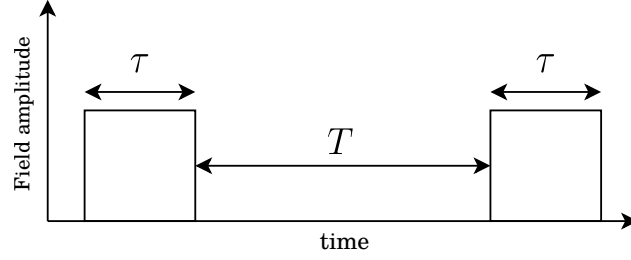

Figure 2.4: The coherent quantum beat measurement sequence consists of two π-pulses of width τ separated by a free-evolution time T. The y-axis is the amplitude of the electromagnetic field (either $\mathcal{E}$- or $\mathcal{B}$-field, depending on the specific transition).

The CQB sequence, shown in Fig. 2.4, consists of two pulses of width $\tau = \pi/\Omega$ at a frequency $\omega = \omega_0$, separated by a variable time interval T. The first pulse performs the same role as in traditional quantum beat spectroscopy, creating a coherent superposition of the two states of spectroscopic interest, $|\psi(0)\rangle = \alpha|e_1\rangle + \beta|e_2\rangle$. During the free evolution time T the superposition evolves to $|\psi(T)\rangle = \alpha|e_1\rangle e^{+i\omega_e T/2} + \beta|e_2\rangle e^{-i\omega_e T/2}$. Since there is no spontaneous emission in this scenario, the second π-pulse serves to project part of the e_1, e_2 superposition back to $|g\rangle$ and closes the quantum-state interferometer. Thus, the system returns to $|g\rangle$ after a free-evolution time T that is an integer multiple of $2\pi/\omega_e$. A final measurement of the population in $|g\rangle$ as a function of T yields the energy difference ω_e. The ground state population, P_g, can be measured by, e.g., exciting the atoms on an optical transition and measuring the absorption or fluorescence. This interference pattern is the basic building block of CQB.

To understand the CQB sequence in the presence of inhomogeneous broadening, we begin by describing the three-level system using the following Hamiltonian in the $|g\rangle, |e_1\rangle, |e_2\rangle$ basis:

$$H = \begin{pmatrix} 0 & \frac{\Omega}{\sqrt{2}}\cos(\omega t) & \frac{\Omega}{\sqrt{2}}\cos(\omega t) \\ \frac{\Omega}{\sqrt{2}}\cos(\omega t) & \omega_0 - \frac{\omega_e}{2} & 0 \\ \frac{\Omega}{\sqrt{2}}\cos(\omega t) & 0 & \omega_0 + \frac{\omega_e}{2} \end{pmatrix} \approx \begin{pmatrix} 0 & 0 & 0 \\ 0 & \Delta - \frac{\omega_e}{2} & 0 \\ 0 & 0 & \Delta + \frac{\omega_e}{2} \end{pmatrix} + \begin{pmatrix} 0 & \frac{\Omega}{2\sqrt{2}} & \frac{\Omega}{2\sqrt{2}} \\ \frac{\Omega}{2\sqrt{2}} & 0 & 0 \\ \frac{\Omega}{2\sqrt{2}} & 0 & 0 \end{pmatrix}, \quad (2.3)$$

where we have applied the usual rotating-wave approximation in the last step.

We define the propagators $D_0(t, t_0) = e^{-iH_0(t-t_0)}$ and $D(t, t_0) = e^{-iH(t-t_0)}$. An initial state $|\Psi_i\rangle$, after evolving through the CQB sequence, turns into $|\Psi_f\rangle = D(T + 2\tau, T + \tau) D_0(T + \tau, \tau) D(\tau, 0) |\Psi_i\rangle$. If the system is initially in the state $|\Psi_i\rangle = |g\rangle$, the population $P_g = |\langle g|\Psi_f\rangle|^2$ at the end of the sequence (with perfect π-pulses, $\tau = \pi/\Omega$) can be analytically calculated to be

$$P_g\left(\tau = \frac{\pi}{\Omega}, T, \Delta\right) = \frac{1}{2}\left\{1 + \cos(\omega_e T) - 4\left(\frac{\omega_e}{\Omega}\right)\cos\left(\frac{\pi\Delta}{2\Omega}\right)\sin(\omega_e T)\right\} + \mathcal{O}\left(\frac{\Delta}{\Omega}\right)^2 + \mathcal{O}\left(\frac{\omega_e}{2\Omega}\right)^2. \quad (2.4)$$

The results with pulse imperfections are discussed in Ref. [4]. As expected, the ground-state population as a function of the pulse length T shows modulations at the desired frequency difference ω_e. We next examine the role of inhomogeneous broadening of the resonance frequency ω_0, or equivalently, the detuning Δ.

Three-level system with inhomogeneous broadening

We first present an intuitive sketch of how CQB works despite inhomogeneous broadening. Note that inhomogeneous broadening affects the coherent superposition $|\psi(0)\rangle = \alpha|e_1\rangle + \beta|e_2\rangle$ prepared by the first pulse, because the amplitudes α and β depend on the generalized Rabi frequency $\Omega' = \sqrt{\Omega^2 + \Delta^2}$. But the

values of α and β do not change the phase accumulated during the free-evolution time T. The measurement of ω_e relies only on the phase accumulated, and so it is not significantly affected by the statistical distribution of ω_0 values over the inhomogeneous width Γ_{inh}.

To see this effect quantitatively, we consider a normal distribution of values of Δ (with mean Δ_0 and full width at half-maximum Γ_{inh}) and average P_g from Eq. (2.4) over this distribution. The ensemble-averaged ground-state population is

$$\left\langle P_g \left(\tau = \frac{\pi}{\Omega}, T, \Delta \right) \right\rangle = \frac{1}{2} \left\{ 1 + \cos\left(\omega_e T\right) - 4 \left(\frac{\omega_e}{\Omega}\right) \cos\left(\frac{\pi\Delta_0}{2\Omega}\right) \exp\left[-\frac{\Gamma_{\mathrm{inh}}^2}{16\ln 2} \left(\frac{\pi}{2\Omega}\right)^2 \right] \sin\left(\omega_e T\right) \right\}. \quad (2.5)$$

We find that the fringes in $\langle P_g \rangle$ are largely independent of Δ_0 and Γ_{inh}. The parameters of the inhomogeneous distribution affect the amplitude of the $\sin(\omega_e T)$ term in Eq. (2.5), which results in an overall fringe shift but *does not change* the periodicity of the oscillations as a function of T. Therefore, ω_e can be extracted by measuring the dependence of $\langle P_g \rangle$ on T. Importantly, the energy difference ω_e can be cleanly measured despite overwhelmingly larger inhomogeneous broadening, $\Gamma_{\mathrm{inh}} \gg \omega_e$.
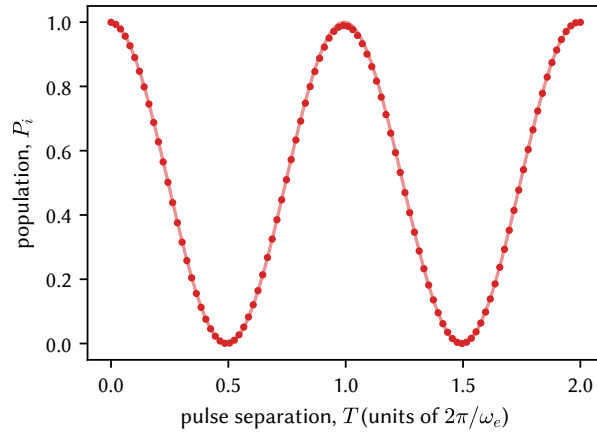

Figure 2.5: Population in the ground state (points) after a resonant CQB sequence for different free-evolution times, in the presence of inhomogeneous broadening of the $g \to e_i$ transitions. The simulation parameters were $\omega_0 = 1$, $\Omega = 10^{-2}$ and $\omega_e = 10^{-4}$. The population traces were averaged over $N = 100$ samples for the detuning Δ drawn from a normal distribution with zero mean and width $\Gamma_{\mathrm{inh}} = 1 \times 10^{-3}$. The solid line through the points is the analytic expression shown in Eq. (2.5).

This feature of CQB can be confirmed using numerical simulations without approximations. Fig. 2.5 shows the results of a CQB sequence applied to an ensemble of three-level atoms whose ω_0 values were drawn from a normal distribution with width Γ_{inh}. There is excellent agreement with our analytical model, showing that coherent quantum beats in the ensemble-averaged ground-state population persist despite inhomogeneous broadening.

In the above discussion, we assumed for analytical ease that the detuning Δ (and therefore also the broadening Γ_{inh}) was small compared to the Rabi frequency Ω. In Ref. [4], we further show that CQB works in the regime of "weak" excitation, where the power broadening is much smaller than the inhomogeneous broadening: $\Omega \ll \Gamma_{\mathrm{inh}}$. Remarkably, in this regime, CQB can be applied with rapid adiabatic passage (RAP) pulses (see Ref. [74]) to produced well-defined oscillations in the ground-state populations after the sequence, allowing ω_e to be measured exactly as before.

Four-level systems with incoherent mixtures

The foregoing discussion of the CQB technique has been based on the three-level V-type system shown in Fig. 2.3 to ease analytical calculations and offer intuitive descriptions. But our application involves the four-level system of $\{|a\rangle, |\bar{a}\rangle, |b\rangle, |\bar{b}\rangle\}$, so we examine whether a similar technique can be made to work in a four-level system.
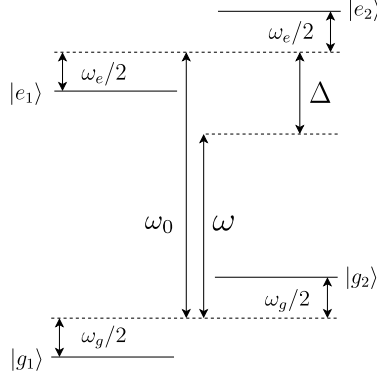

Figure 2.6: A system of four levels, where the energy differences of interest (ω_g, ω_e) are measured using spectroscopy of the $g_i \to e_j$ transitions $(i, j = 1, 2)$. The frequency of light is ω and the average of the $g_i \to e_j$ resonance frequencies is ω_0.

Consider the system of four states in Fig. 2.6, where the two ground states $\{|g_1\rangle, |g_2\rangle\}$ are separated by ω_g and the two excited states $\{|e_1\rangle, |e_2\rangle\}$ are separated by ω_e, assuming that $\omega_g, \omega_e \ll \omega_0$. We further assume that the ground states $|g_1\rangle$ and $|g_2\rangle$ are initially populated and are in thermal equilibrium at a temperature $T_{\text{spin}} \gg \omega_g/k_B$, so that the density matrix is initially in the mixed state $\rho(0) = 1/2|g_1\rangle\langle g_1| + 1/2|g_2\rangle\langle g_2|$. To understand the effect of the CQB sequence on such mixed states, we numerically evolve the density matrix ρ of the four-level system through the CQB pulse sequence, with the four-level Hamiltonian

$$H = \begin{pmatrix} -\frac{\omega_g}{2} & 0 & \frac{\Omega}{2}\cos(\omega t) & \frac{\Omega}{2}\cos(\omega t) \\ 0 & +\frac{\omega_g}{2} & \frac{\Omega}{2}\cos(\omega t) & \frac{\Omega}{2}\cos(\omega t) \\ \frac{\Omega}{2}\cos(\omega t) & \frac{\Omega}{2}\cos(\omega t) & \omega_0 - \frac{\omega_e}{2} & 0 \\ \frac{\Omega}{2}\cos(\omega t) & \frac{\Omega}{2}\cos(\omega t) & 0 & \omega_0 + \frac{\omega_e}{2} \end{pmatrix}. \tag{2.6}$$

Here we assume that the pulses couple each ground state to the two excited states with equal matrix elements, so that $\Omega = \frac{1}{2}\langle e_i|H_{\text{int}}|g_j\rangle$ $(i, j = 1, 2)$. These assumptions are well-justified for the two Kramers pairs $a, \bar{a}$ and $b, \bar{b}$ in our system (see Appendix A).

Fig. 2.7 shows the effect of the CQB sequence on a four-level atom when $\Delta = 0$. Despite starting from the mixed state $\rho(0)$, the pattern of fringes in the ground state population at the end of the sequence shows beats at both ω_e and ω_g, allowing both energy differences to be measured. This elucidates a more general and surprising feature: the CQB method can work in four-level systems without requiring the ground states to be prepared in coherent superpositions. This feature greatly simplifies the measurement process, leading to experimental simplicity and improvements to the duty cycle of measurements. We further verified that CQB works when inhomogeneous broadening of the $g_i \to e_j$ transitions is included, in the regime $\Omega > \Gamma_{\text{inh}} > \max\{\omega_e, \omega_g\}$. The calculations in Fig. 2.8 for a distribution of resonance frequencies demonstrate that clear fringes in $\langle P_g \rangle$ are obtained despite broadening, and that the *entire ensemble* contributes to the measurement of the small energy differences ω_g, ω_e.
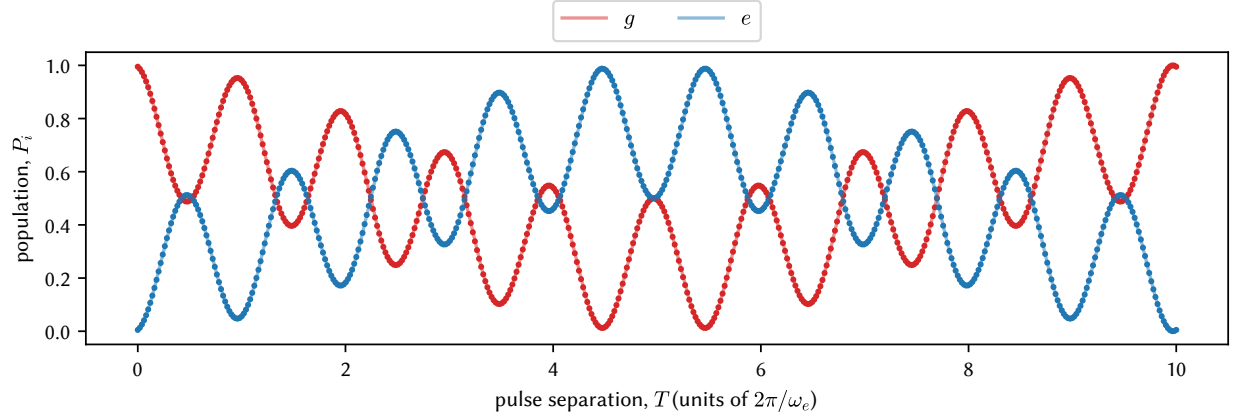
Figure 2.7: Populations in a four-level system after a resonant CQB sequence for varying free-evolution times. g (e) denote the summed populations of both ground (excited) states. The simulation parameters were $\omega_0 = 1$, $\Omega = 10^{-2}$, $\omega_e = 10^{-3}$, $\omega_g = 10^{-4}$, and $\Delta = 0$.
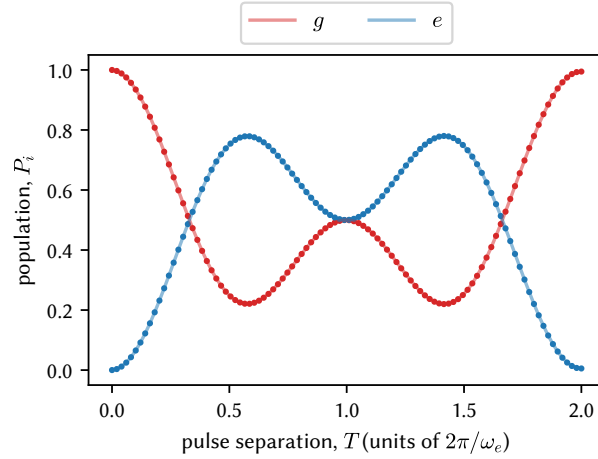

Figure 2.8: Populations in a four-level system after a resonant CQB sequence for varying free-evolution times, in the presence of inhomogeneous broadening of the $g_i \to e_j$ transitions. The simulation parameters were $\omega_0 = 1$, $\Omega = 10^{-2}$, $\omega_e = 10^{-4}$, and $\omega_g = 5 \times 10^{-5}$. A set of $N = 100$ samples of the detuning Δ were drawn from a zero mean normal distribution with width $\Gamma_{\text{inh}} = 2.5 \times 10^{-3}$.

2.4.2 Sensitivity of the technique

The CQB technique amounts to mapping out an ω_e and/or ω_g fringe by varying T, while keeping τ and Δ fixed, and then fitting a sinusoid to the periodic modulation of the ground-state population. This procedure may seem qualitatively different from conventional spectroscopy techniques such as Ramsey interferometry, where the field detuning is usually the parameter that is varied. Nonetheless, the two techniques have comparable fundamental limits to their precision. For CQB the attainable precision is [75]

$$\delta\omega_{\text{CQB}}/2\pi = \frac{1}{\pi\mathcal{S}}\sqrt{\frac{6}{T_{\text{int}}T}}, \tag{2.7}$$

where T_{int} is the total integration time and $\mathcal{S}$ is the signal-to-noise ratio of a measurement. Here we have assumed that a measurement is made once every pulse separation time T (i.e. $T \gg \tau$). In contrast, the

Ramsey spectroscopy technique is capable of precision

$$\delta\omega_{\text{Ramsey}}/2\pi = \frac{1}{2\mathcal{S}}\sqrt{\frac{1}{T_{\text{int}}T'}}, \tag{2.8}$$

where T' is the separation between the oscillatory pulses in the Ramsey sequence.

There are two important sensitivity advantages to the CQB technique, as evident from Eq. (2.7) and (2.8). First, note that $\delta\omega$ in both cases improves $\propto 1/\mathcal{S}$. To measure an energy difference masked by inhomogeneous broadening using Ramsey interferometry, the linewidth must be narrowed in some way so that the $g \to e_i$ transitions are distinguishable by the state readout transition (with inhomogeneous width Γ'_{inh}). In solid-state systems, techniques such as spectral hole-burning [76] can yield lines narrower than the inhomogeneous width, but always at the expense of signal-to-noise because only a fraction $\sim \frac{2\omega_e}{\Gamma'_{\text{inh}}}$ of the atoms in the ensemble are selected. Meanwhile, *all* the atoms in the ensemble contribute to the CQB signal, resulting in significantly higher signal-to-noise $\mathcal{S}$ in precision measurements.

Second, in order to minimize $\delta\omega$, the free evolution time (T in CQB, and T' in Ramsey) must be maximized. The free evolution time can be increased without signal loss up to the ensemble phase coherence time. In Ramsey spectroscopy, the ensemble coherence time $T_2^* \sim 1/\Gamma_{\text{inh}}$ is limited by the broadening of the $g_i \to e_j$ transition frequency ω_0. In contrast, the CQB method is insensitive to Γ_{inh}. The evolution time T is limited only by the coherence time T_2 of the superposition of states g_i or e_j, not the $g_i - e_j$ superpositions. Therefore the spectroscopic resolution improves as $\delta\omega \sim 1/\sqrt{T_2}$ rather than $\sqrt{\Gamma_{\text{inh}}}$. Taken together, these two advantages can lead to significant improvements, by a factor $\mathcal{X} = \pi\sqrt{\frac{\Gamma_{\text{inh}}\Gamma'_{\text{inh}}T_2}{12\omega_e}}$, compared to the Ramsey method.

The advantages of the CQB technique make it especially well-matched to precision solid-state spectroscopy because (a) Γ_{inh} and Γ'_{inh} can be large, and (b) T_2 can be much longer than the ensemble coherence time $T_2^* \sim 1/\Gamma_{\text{inh}}$. We consider the implications on the four-level system involved in our measurement: $\{|a\rangle, |\bar{a}\rangle, |b\rangle, |\bar{b}\rangle\}$. The $\{a, \bar{a}\} \to \{b, \bar{b}\}$ hyperfine transitions are inhomogeneously broadened ($\Gamma_{\text{inh}}^{\text{hfs}} \sim 70$ kHz [36]), presenting a challenge to the measurement of $\nu_{a\bar{a}}$ without applying large magnetic fields or compromising on the number of atoms interrogated. However, the hyperfine states have notably long coherence times ($T_2 \sim 15$ ms) as measured through hole-burning spectroscopy [77]. From a free evolution time of $T = T_2 \approx 15$ ms with CQB as compared to $T' = T_2^* \sim 1/\Gamma_{\text{inh}}^{\text{hfs}} \approx 2\,\mu s$ with Ramsey, there is a $\sim 55\times$ improvement in precision. We further estimate that $10^3\times$ more atoms from the ensemble can be used in the CQB measurement by relaxing the required linewidth of spectral holes used for optical population readout with a 1 G bias field, leading to an overall improvement in $\delta\omega$ by about 3 orders of magnitude.

Chapter 3

Apparatus design

In this chapter, I describe the development of the apparatus for the **O**ctupole-deformed **N**uclei **I**n a **Cryst**al (ONIX) experiment proposed in Chapter 2. A schematic of the setup is shown in Fig. 3.1. This apparatus was built from the ground up over the course of this MSc with a combination of new equipment and recycled equipment from previous experiments in the lab. As in the figure, the apparatus can be broadly segmented into components that stabilize the frequency of the laser (Section 3.1), vary the frequency and amplitude of the laser and detect laser absorption by the crystal (Section 3.2), control the environment around the Eu:YSO crystal (Section 3.3), and precisely control the timing between different hardware to realize particular measurement sequences (Section 3.4). The sections that follow will address each of these functionalities to provide context but will provide more detail on aspects that I was substantially involved in developing.
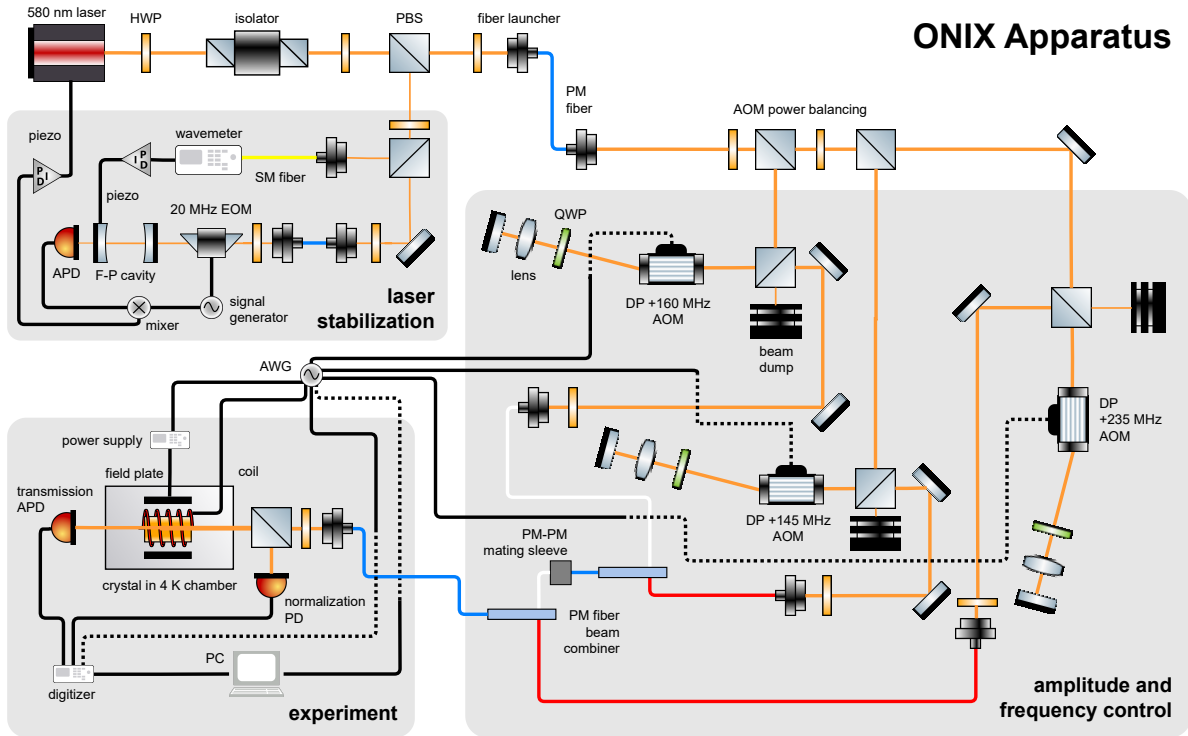

Figure 3.1: A schematic representation of the apparatus for the ONIX experiment. The acronyms used are defined throughout this chapter. AOM frequency shifts are listed as e.g. "DP 160 MHz", which refers to an overall +160 MHz shift obtained by the first order diffracted beam in a double-pass AOM configuration.

3.1   Laser stabilization

All measurements in this experiment involve laser absorption through the crystal, so the stability of the laser is an important consideration for making high-quality measurements. We use a commercial laser system from Vexlum Ltd. that includes a vertical-external-cavity surface-emitting laser (VECSEL) frequency-doubled via second-harmonic generation (SHG) to 580 nm. This system outputs up to 2 W at 580 nm, which easily satisfies the power requirements for all of our measurements. The frequency of this laser is finely tuned (within ~ 10 GHz) by adjusting the applied voltage on a piezoelectric transducer (abbr. piezo) that modulates the length of an external feedback cavity inside the system.

For broadband or lower-precision measurements, such as optical absorption spectra (Section 4.1), we stabilize the laser by measuring its frequency with a HighFinesse wavemeter (~ 1 MHz resolution) and applying proportional and integral feedback to the laser piezo based on the frequency deviation from a desired setpoint. This stabilizes the laser to a linewidth of < 2 MHz over many hours.

As shown in Fig. 3.1, for high-precision measurements, such as hyperfine state preparation (Section 4.4), we use two feedback loops. We first stabilize the laser using the transmission signal through a Thorlabs SA200-5B scanning Fabry-Pérot (F-P) interferometer (free spectral range of 1.5 GHz and resolution of 7.5 MHz). This optical cavity is enclosed within a small vacuum chamber. The chamber is held at $\sim 10^{-7}$ Torr by an ion pump in order to suppress drifts and fluctuations from temperature changes and air currents. We send ~ 10 uW of light through the cavity and detect the transmitted light with a fast avalanche photodiode (APD). We use a modified version of the Pound-Drever-Hall technique [78], detecting the light that is transmitted rather than reflected, to stabilize the laser with this setup.

We use the hardware shown in Fig. 3.1 to generate a linear error signal, indicating the deviation of the laser frequency from a nearby cavity mode. We apply phase modulation to the light entering the cavity with a 20 MHz resonant electro-optic modulator (EOM), which is driven by a signal generator. While periodically sweeping the laser piezo voltage over a sufficient range to see a cavity transmission peak, we adjust the amplitude of the 20 MHz signal until first- and second-order sidebands of the main peak are clearly visible, as shown in Fig. 3.2 in yellow. Next, as in Fig. 3.1, we use the same signal generator to generate an additional 20 MHz signal at a defined phase offset relative to the EOM driving signal. To obtain a derivative lineshape to use as an error signal, we feed both the additional 20 MHz signal and the transmission signal through a radiofrequency (rf) mixer and lowpass filter the mixer output at ~ 1 MHz. After optimizing amplitudes and phases, the resulting signal is shown in blue in Fig. 3.2.
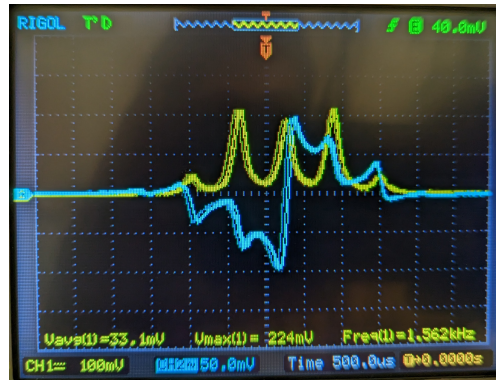

Figure 3.2: Transmitted light signal (yellow) and error signal (blue) through a Fabry-Pérot cavity as its length is modulated with a triangle wave.

Next, a summer undergraduate student – Daniel Stedman – fed this error signal to a Moku:Go controller to apply proportional, integral, and derivative (PID) feedback to the laser piezo. With this setup, after

optimizing rf amplitudes and phases, he was able to lock our laser to a linewidth of 10.1 kHz relative to the cavity. This was measured by analyzing the spectral noise in the error signal while the laser is locked, as shown in Fig. 3.3.
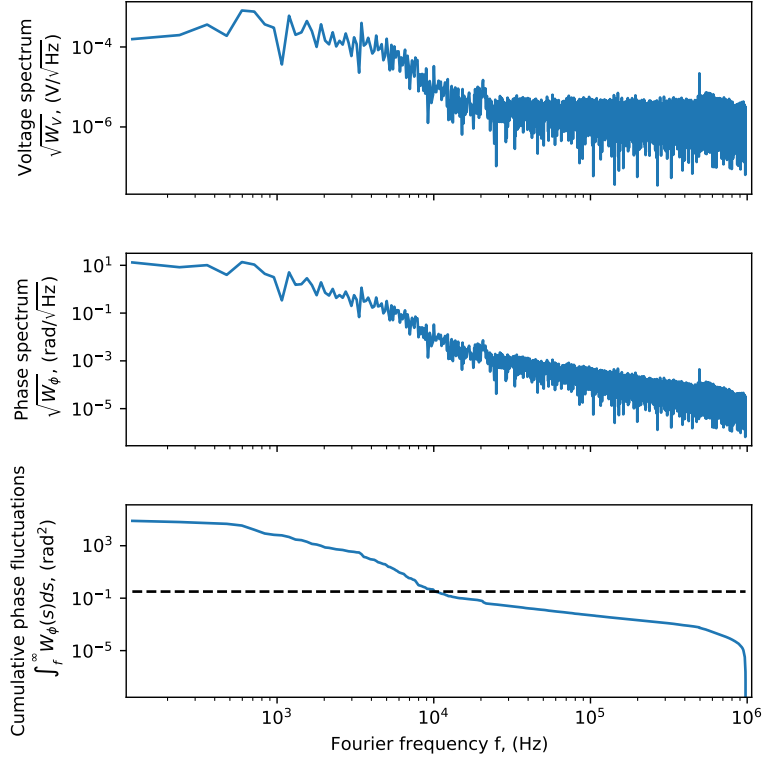

Figure 3.3: Voltage (top) and phase noise (middle) spectra of the error signal when the laser is locked to a Fabry-Pérot cavity. The integrated phase fluctuations (bottom) indicate a laser linewidth of 10.1 kHz.

This first feedback loop stabilizes the laser only in reference to the cavity. Although the cavity is meant to be a stable reference with minimal frequency fluctuations, there can still be drifts due to temperature variations. Further, this first loop only allows the laser to be locked in steps of the cavity free-spectral range of 1.5 GHz, which could be off-resonance from the optical transition of the atoms in the crystal. For control over absolute frequencies and suppression of drifts, we then stabilize the cavity frequency relative to our wavemeter, which serves as a good absolute frequency reference. To do so, we read the frequency of the laser with the wavemeter and apply corrections to the piezo on one of the cavity mirrors, adjusting its length and thus its frequency. This allows us to vary the frequency of the laser within a ~ 10 GHz range around 516847.5 GHz (the optical resonance) while maintaining a 10 kHz linewidth on fast timescales and absolute frequency stability within the wavemeter resolution of 1 MHz.

3.2   Optics

In addition to being stable, the laser frequency and intensity need to be controlled in particular ways in order to facilitate the $\mathcal{T}$-violation experiment. Broadly, the laser has two primary functions:

1. efficiently prepare the Eu^{3+} ions in particular hyperfine ground states

2. efficiently read out the populations in particular hyperfine ground states with high precision and accuracy

As described in Section 2.2, to provide these functions, we need to imprint three rf sidebands on the laser and have control over the frequencies and amplitudes of those sidebands. When we say "efficient" here, we mean that the impact on the measurement duty cycle and signal-to-noise ratio (SNR) should be minimized. Instead, limitations from the atoms, such as their coherence times and shot noise, should dominate. Thus, the frequency and amplitude control needs to be fast, with response times on the order of microseconds, in comparison with the millisecond to ten-millisecond scale coherence times of the atoms. The detection scheme must also allow for measurements on this timescale, eventually with a shot-noise-limited technique to deliver the projected sensitivity described in Section 2.3.

3.2.1   Amplitude and frequency control

To obtain fast amplitude and frequency control, we use acousto-optic modulators (AOMs), as shown in Fig. 3.1. These devices contain a crystal and a piezoelectric transducer within a resonant circuit, which is driven at an rf frequency (typically ~ 100 MHz). The laser is aligned through the crystal in such a way that Bragg diffraction occurs when the device is driven with rf. The diffraction pattern contains beams of various orders spatially offset from the initial, central beam, each at well-defined frequency shifts corresponding to integer multiples of the rf frequency depending on the order of the beam. For an 80 MHz AOM, for instance, the $+1$ order beam is shifted by $+80$ MHz relative to the 0 order beam. AOMs can be rather efficient, coupling up to ~ 85 % of incident power into one first-order beam. The amplitude and frequency of a diffracted AOM beam can be controlled via the amplitude and frequency of the driving rf signal, which can be finely and quickly adjusted with e.g. an arbitrary waveform generator (AWG). AOMs can have sub-microsecond response times, allowing for sequences with optical control on those timescales.

When using AOMs for frequency control, one complication is that the rf frequency affects the pointing of the beam through the diffraction pattern. To maintain stable pointing of the beam on the experiment, we couple the output beam from the AOM to an optical fiber before aligning the beam onto our crystal. In that case, however, the output power to the experiment would drastically change depending on the rf frequency sent to the AOM. We define the *bandwidth* of an AOM setup as the frequency width over which the output power from a fiber stays within 50% of its peak value. To obtain higher bandwidths, we instead use our AOMs in a double-passed (DP) configuration, where the first-order diffracted beam is retro-reflected back into the AOM. In doing so, the beam is also frequency shifted by two times the first order shift. The setup for this is shown in Fig. 3.1. Since the incident light on the AOM is linearly polarized by a polarizing beam splitter (PBS) and there is a quarter waveplate (QWP) in the diffracted beam path, the retro-reflected beam passes through the QWP twice so that its linear polarization is rotated by 90 degrees. The outgoing beam is thus sent in a different direction than the incident beam by the PBS.

The simplest setup for a double-pass configuration would be to place one plane mirror to retro-reflect the diffracted beam. However, since the diffracted beam angle depends on the rf frequency, the retro-reflection would become misaligned from the incident beam as the rf frequency is adjusted away from the frequency at which the mirror was aligned. For more versatile retro-reflection, we place a cat's eye (a plane mirror with a lens a focal length away) in the diffracted beam path, as shown in Fig. 3.1. A cat's eye returns incident light at the same angle at which it was incident. However, it does not return light at the same distance from the optical axis at which it was incident, so the bandwidth of the setup is still limited by beam-pointing changes. To further increase the bandwidth, we place the lens in the cat's eye one focal length away from the center of the AOM along the optical axis. In doing so, if we treat the diffraction as occurring at a point source located at the center of the AOM, the reflected beam will have the same angle and position as the incident beam regardless of rf frequency. The bandwidth of the device is then limited only by the bandwidth of the resonant rf circuit in the AOM, not by the spatial diffraction pattern. For a detailed study of AOM

diffraction efficiencies and bandwidths under various double-pass configurations, consult Ref. [79].
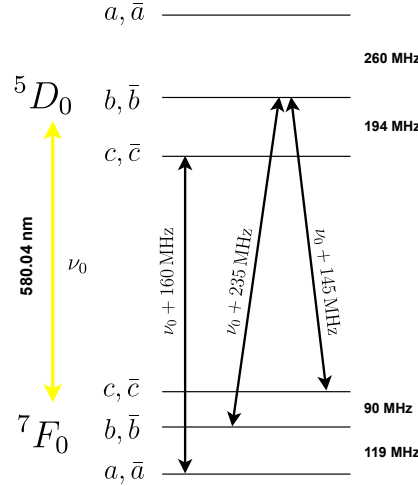

Figure 3.4: $^7F_0 \rightarrow {}^5D_0$ level diagram showing the particular states addressed by rf sidebands imprinted by the AOMs for a spectral class that is resonant with all three optical frequencies.

We use three AOMs at particular frequencies in our optical setup in order to optically address particular hyperfine states, as shown in Fig. 3.4. This choice of frequencies facilitates hyperfine state preparation, as described in Sections 2.2 and 4.4. The power ratios between them are controlled by a pair of half-waveplates. Although the power ratios are relevant to the experiment, we do not use motorized waveplate mounts. Since we have plenty of laser power, we can adjust the incident power from each AOM on the crystal by adjusting the amplitude of the rf signal driving the modulator. On all three of our AOMs, we obtain double-passed diffraction efficiencies near 50%. With the carefully placed cat's eye setup, we obtain post-fiber double-passed AOM bandwidths of roughly 30 MHz around each of our three AOMs' specified center frequencies: 80 MHz, 80 MHz, and 115 MHz. As labeled in Fig. 3.1, we drive our three AOMs at 80 MHz, 72.5 MHz, and 117.5 MHz, respectively, in order to address particular hyperfine states within the optical transition.

Beam combining

Our setup of three AOMs provides us with independent frequency and amplitude control over three distinct laser beams. In our measurement scheme, we must be able to address the exact same group of atoms with any combination of these three beams. Such sequences are necessary to prepare the atoms in particular hyperfine states. Thus, we must precisely spatially overlap each of the three beams from our AOMs.

To combine our three beams with standard optics, the solution is to polarize the beams differently and use polarizing beam splitters to co-align all three beams onto a single polarization-maintaining (PM) fiber. To provide enough degrees of freedom and simplify alignment, we can assign two mirrors to each beam that are independent of the other two beams. With only one lens focusing light onto the fiber, however, this setup does not provide independent spatial mode matching for each beam, which leads to losses in efficiency. Although one could imagine adding an independent lens to each beam path, the selection and adjustment of each lens would be challenging. We tried this co-aligned single-fiber setup, but found that the fiber coupling efficiency and alignment stability were inadequate.

Instead, we now use three-port PM fused fiber polarization combiners (Thorlabs PFC635A), which combine two beams from separate fibers into a single fused fiber, without relying on polarizing optics. As shown in Fig. 3.1, we use two combiners to combine our three beams. Although these combiners are rated for 620 - 650 nm, we found them to work adequately at 580 nm, with the compromise of a 60% insertion loss through one of the input ports (and < 2% on the other). With a high-quality 580 nm test beam, we observed a 75% coupling

efficiency through one port and 27% through the other. This setup is preferred, despite the insertion loss, because the alignment is more stable and the post-AOM coupling efficiencies are much better with individual fiber launchers and correspondingly better spatial mode matching. In practice, with the spatially distorted beams that exit our AOMs, we obtain a ~ 16 % coupling efficiency through the worse port and a ~ 25 % coupling efficiency through the better one.

Possible upgrade: electro-optic modulators

In the near future, we will explore the possibility of replacing our entire three AOM setup with a single broadband fiber EOM. In contrast with acousto-optic devices, electro-optic phase modulators can imprint rf sidebands on light without affecting their spatial alignment. As a consequence, however, they are usually incapable of imprinting only a single rf sideband on the laser. Although the optical power in the first-order sideband can be optimized by adjusting the driving rf power, both the positive and negative sidebands will be present, which can have undesired consequences on state preparation.

However, if the EOM is driven with a sawtooth waveform ("serrodyne modulation") rather than a sinusoidal waveform, it is possible to suppress the optical power in all but one rf sideband (e.g. the +1 order) to $\lesssim 0.2$ % of the power in the dominant sideband [80]. Compared to a sinusoid at a given frequency, a sawtooth waveform contains contributions from higher harmonics, imposing a high bandwidth requirement to realize a serrodyne modulation system.

Recent advances in photonics have brought broadband fiber-based phase modulation technology to optical wavelengths. We purchased a 580 nm fiber-based electro-optic phase modulator with a 10 GHz bandwidth from AdvR Inc. In our current experiments, we use an arbitrary waveform generator with a 625 MHz sampling rate and a 200 MHz bandwidth to drive our AOMs (details in Section 3.4). This AWG is capable of applying clean, single-order rf sidebands within the 90 MHz range required for our experiment (we use 145 - 235 MHz for our AOMs, but only the relative detunings of the beams are important). A serrodyne modulation setup would allow us to use a single rf-channel of the AWG to completely implement the desired frequency and amplitude control of our laser. The single channel could either sequentially output different desired rf sidebands or simultaneously apply them through the superposition principle. This setup would greatly reduce the complexity of the optics for the experiment, likely improving polarization and intensity stability of the light as a consequence.

3.2.2   Detection setup

After the beams have been spatially overlapped, they are sent to the experiment, as shown in Fig. 3.1. Using a PBS, we deliver light to the crystal from all three beams, such that it is polarized along the D_1 axis of the crystal and propagates along the b axis. This is the polarization scheme that gives the strongest absorption for the ions in site 1 of the crystal [38], which we seek to address. We adjust the pre-crystal half waveplate (HWP) and power balancing half waveplates to ensure adequate power is incident on the crystal from each beam.

When scanning over spectral hole features in measurement sequences, as described in Chapter 4, we typically step the laser frequency sequentially with our AOMs, pulsing the laser on at each frequency for $\sim 500\,\mu$s at incident powers below $5\,\mu$W. These power and timing parameters are chosen to reduce spectral hole-burning effects during the scan itself. For these low powers and fast timescales, we use an avalanche photodiode (Thorlabs APD130A) to detect the transmitted light through the crystal. Since many of our experiments involve adjusting AOM frequencies, the incident power on the crystal varies substantially, affecting the size of the transmission signal. For this reason, we place a second photodiode (Thorlabs PDA36A2) on the other port of the PBS before the crystal to serve as a proxy for the incident light on the crystal. We use

this photodiode to normalize the signals for all our measurements. We use 580 nm bandpass filters (Thorlabs FBH580-10) on both the transmission and normalization photodiodes to filter out background light.

This detection setup was used for all measurements in this report, but it is susceptible to polarization fluctuations of the laser. We have recently observed polarization fluctuations when high powers (> 100 mW) are incident on our PM fibers. As will be discussed in Chapter 4, this is a possible explanation for why certain features in our measurements are distorted despite their small error bars. In the future, we will remove the first PM fiber in our setup to suppress polarization fluctuations and use a 50/50 beamsplitter after the final PBS to ensure more accurate normalization.

3.3   Hardware

To implement the scheme described in Section 2.2, beyond control and stability of the laser, there are several additional technical requirements related to the environment around the crystal. These requirements are:

(a) maintain the crystal at cryogenic temperatures to obtain long hyperfine coherence times;

(b) ensure optical access for absorption measurements;

(c) apply a strong rf magnetic field to efficiently drive the $^7F_0$ hyperfine transitions;

(d) apply and quickly switch on/off small static electric fields in order to efficiently read out populations in different orientations of ions;

(e) and apply a small static magnetic field to break the degeneracies between Kramers pairs.

Specific bounds on the temperatures, field strengths, and timescales imposed by these requirements will be provided and justified in the subsections that follow. We note that these requirements are relatively easy to satisfy independently but difficult to satisfy simultaneously. For instance, although other research groups have designed apparatuses to apply static electric fields to the crystal [42] or to simultaneously apply static and rf magnetic fields [48, 39], no previous experiment has needed to apply all three of these fields at once. This synthesis presents the main technical challenge of the ONIX experiment at this initial stage.

3.3.1   Temperature considerations

To maximize the sensitivity of the experiment as described in Eq. 2.2, the crystal must be cooled to cryogenic temperatures to lengthen coherence times and suppress broadening effects. I now discuss the various temperature-dependent properties of this crystal in order to bound the desired temperature range for the crystal.

The crystal exhibits certain temperature-dependent properties because of the presence of phonons: quanta of vibrational energy within the lattice, which disturb atomic states. Phonons are suppressed in accordance with Bose-Einstein statistics as the temperature is decreased. There are two phonon-mediated processes that contribute to the broadening and decoherence of $^7F_0$ hyperfine levels in this crystal: inelastic Raman scattering and the two-phonon Orbach process [41]. Inelastic Raman scattering involves the absorption and emission of a high energy phonon to a lower energy phonon (or vice versa) via a hyperfine level and virtual energy level. The two-phonon Orbach process involves phonon absorption from a $^7F_0$ hyperfine level into $^7F_1$, followed by phonon emission into a different $^7F_0$ hyperfine level [41]. In contrast, direct phonon absorption or emission between $^7F_0$ hyperfine levels is negligible because of the low phonon density of states at the < 210 MHz hyperfine splittings.

$^7F_0$ hyperfine state population measurements in Eu:YSO are limited, first, by the spectral hole lifetime T_1, which sets the upper bound on the measurement cycle time. T_1 decreases with temperature T due to the two-step Orbach process and inelastic Raman scattering, which dominates below ~ 12 K [38]. At 2 K, spectral holes have been observed to live for weeks to one month [38]. More restrictively, the $^7F_0$ hyperfine coherence time T_2 places an upper bound on the free-evolution time in the CQB sequence and thus limits the sensitivity of the experiment according to Eq. 2.2. T_2 has been measured to be effectively constant below 16 K [41], where a temperature-independent term due to interactions with ^{87}Y nuclear spins ($I = 1/2$) in the YSO crystal dominates. Above 16 K, the coherence time decreases due to the two-step Orbach process [41].

Naively, then, the upper bound for the temperature of our crystal seems to be 16 K, where $T_2 \sim 15$ ms [54, 55, 41] and $T_1 \sim 200$ ms [38]. Lower temperatures will substantially extend T_1 but not T_2. It would seem that longer T_1 provides little benefit to the experiment, as the hyperfine states will be reset for the next CQB measurement at a faster timescale than that. Practically, however, it would be more challenging to run intermediate experiments demonstrating spectral hole-burning techniques if the hole lifetime were short, as our sequences will not be completely optimized at first. For this reason, lower temperatures will generally make experiments easier.

The homogeneous linewidth $\Gamma_{\mathrm{opt.,hom.}}$ of the $^7F_0$ - $^5D_0$ is another relevant temperature-dependent property because it determines the minimum width of the spectral holes that can be burned. This width, in turn, affects the required lab electric field magnitudes to separately resolve ions in different orientations within the lattice, as described in Section 2.2. $\Gamma_{\mathrm{opt.,hom.}}$ includes summed contributions from the natural radiative lifetime $\tau_{\mathrm{opt.}} = 1/\pi\Gamma_{\mathrm{opt.,hom.}}^{\mathrm{rad.}}$, ^{87}Y nuclear spin interactions $\Gamma_{\mathrm{opt.,hom.}}^{\mathrm{spin}}$, and one- and two-phonon scattering $\Gamma_{\mathrm{opt.,hom.}}^{\mathrm{phonon}}$ [38]. Although $\tau_{\mathrm{opt.}}$ and $\Gamma_{\mathrm{opt.,hom.}}^{\mathrm{spin}}$ are temperature independent, $\Gamma_{\mathrm{opt.,hom.}}^{\mathrm{phonon}}$ (which is dominated by inelastic Raman scattering) scales as T^7 until 35 K [38]. To obtain spectral holes that are ~ 100 kHz wide and thus easily split with small static electric fields, as we assumed in Section 2.3 and Section 3.3.3, the temperature must be below ~ 11 K.

Collectively, these properties demand a maximum temperature of 11 K for the crystal within our apparatus, with clear benefits at even colder temperatures. The most reliable way to bring a solid sample to these temperatures is to enclose it within a vacuum chamber and cool it conductively with a closed-cycle cryocooler. ONIX recycles a vacuum chamber and pulse tube refrigerator (Cryomech PT415) used in a previous experiment, so only a mount for the crystal needed to be designed. The pulse tube provides 1.35 W of second-stage cooling power at 4.2 K while supplying 40 W at 45 K on its first stage. This is an excessive amount of cooling power for a centimeter-scale crystal. The vacuum chamber is equipped with a scroll roughing pump, a turbomolecular pump, and panels with coconut charcoal ("sorbs") for cryo-pumping [81]. This allows the chamber to pump down to $< 10^{-7}$ Torr with the pulse tube running and $< 10^{-5}$ Torr with the pulse tube off. Conductive heat transfer between the outer and internal chamber walls is thus suppressed so that the two stages to reach their specified temperatures.

3.3.2   Crystal mount

To deliver the cooling power of the pulse tube to the crystal, a suitable mount is necessary. Julia Ford and I designed the first iteration of the crystal mount, which we used in our initial experiments. The most stringent constraint on the design comes from the required rf magnetic field strength (> 10 G, explained in Section 3.3.4), which necessitates a small diameter rf coil in a resonant circuit. This leads to a trade-off between decreasing the coil diameter by reducing the size of the mount and decreasing thermal resistance by increasing the size of the mount.

Our first crystal, containing 0.01% Eu by mass doped in YSO with natural abundances of ^{151}Eu and ^{153}Eu (48% and 52%, respectively), is sized as 3.5 mm by 4 mm by 10 mm cut along the dielectric D_1, D_2, and b axes, respectively. Our experiments involve shining light that is polarized along the D_1 axis and propagating along the b-axis. We design the rf coil to wrap around the b axis so that it can enclose the crystal but still allow optical access. Further, as described in Section 2.2, the static electric and magnetic fields must run along the same axis. Based on the measurements in Ref. [42], the largest Stark splittings of spectral holes occurs along the D_1 axis, so we pick that direction for both static fields. This defines the geometric constraints on the crystal mount.

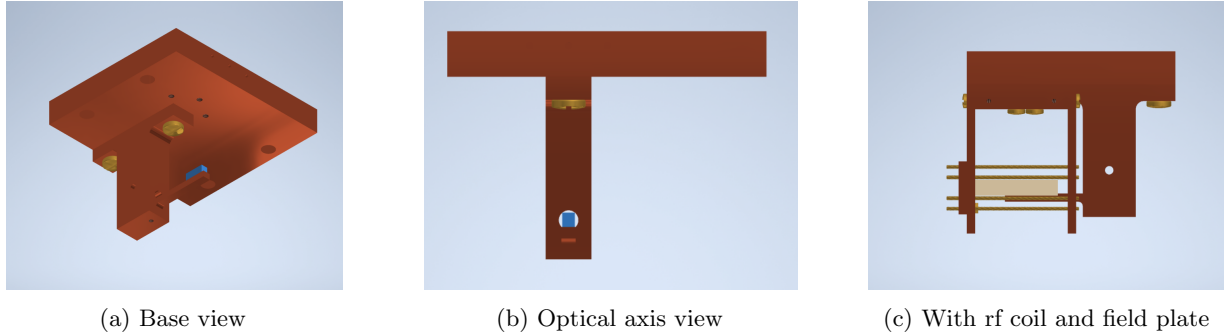(a) Base view   (b) Optical axis view   (c) With rf coil and field plate

Figure 3.5: CAD model of the version 1 crystal mount, shown from various angles. The crystal is depicted in blue. Copper and brass pieces are colored as such.

We made a CAD model of the design, which is shown in Fig. 3.5. Notably, the design places the crystal on a cantilever in order to fit a mount for the rf coil and static electric field plates, shown in Fig. 3.5c. Without the coil and field plates, the design comes in two pieces: an adapter plate for the hole pattern inside the chamber and the actual J-shaped crystal mount. The J-shaped piece was designed such that the end of the cantilever (where there is a hole for a temperature diode) would reach < 6 K based on thermal resistance and heat load calculations for the chamber's internals. To achieve this, the parts were machined out of pure oxygen-free copper (C101). The crystal is fixed to the cantilever using cryovarnish (Lake Shore VGE-7031), which we selected for its strong thermal and mechanical connection and its ability to be removed by bathing in acetone. The thermal resistance of this interface and the thermal conductivity of the crystal itself present the main uncertainties in the thermal performance of this design.

For initial experiments, we assembled this mount without the rf coil and field plates and installed it in our vacuum chamber. We observed that the temperature diode on the mount reached 4.5 K. However, when we burned spectral holes, we observed lifetimes of roughly 0.5 seconds, suggesting that the crystal's true temperature was 15 K [38]. A few weeks later, we were unable to burn spectral holes at all in those same timescales. We eventually discovered that the cryovarnish had delaminated from the crystal for unknown reasons, increasing its temperature. When we re-applied the cryovarnish, we were able to burn spectral holes with similar lifetimes again. However, later on, the cryovarnish delaminated once again. Since this same batch of cryovarnish performs well in other applications in our lab, we suspect that it has issues bonding to

YSO in particular. After the second failure, we decided that we needed a better attachment system for the crystal and a different mount design to improve thermal contact. For this reason, the field plates and coil that we designed for this version of the mount were never used and are thus not discussed in further detail.

The second version of the crystal mount was designed by Julia Ford. I provide a brief overview here as context for subsequent sections of this report, but the details of the design can be found in Julia's thesis [82].
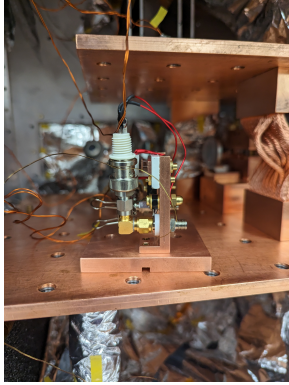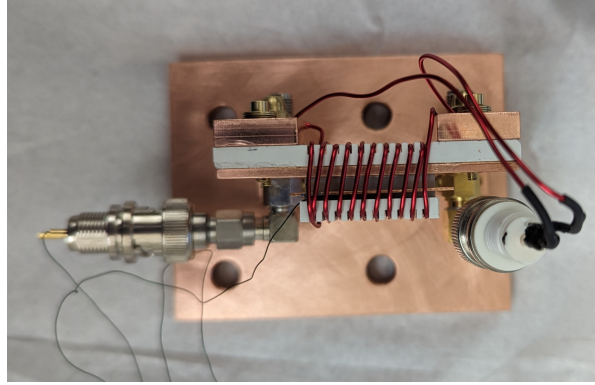
(a) in chamber   (b) overhead

Figure 3.6: Images of version 2 of the crystal mount, after assembly. On the left, the mount is shown inside the chamber, before the final mounting screws were installed. On the right: an overhead view of the assembly.

For experiments with this mount, we used a new, isotopically-enriched Eu:YSO crystal that we purchased. This crystal is doped to 0.01% by mass with ^{153}Eu:YSO and has dimensions of 2.5 mm by 3 mm by 10 mm, along the crystallographic D_1, D_2, and b axes. The isotopic enrichment roughly doubles our signal size, since only the ^{153}Eu (natural abundance 52%) is relevant to our experiment.

As shown in Fig. 3.6, the revised crystal mount is considerably different from the original one, but implements all of the requirements listed at the beginning of Section 3.3. To apply electric fields across the D_1 axis of the crystal, we epoxied thin copper plates to two parallel faces of the crystal. The thicker plate is held at ground while a voltage is applied to the thinner plate. The ground plate also acts as the primary thermal contact surface for the crystal. Notably, we used cryogenic vacuum-appropriate epoxy to make this connection, rather than the cryovarnish that failed us previously. Accounting for the epoxy thickness, the field plate separation is roughly 3 mm. The rf coil (wrapped around the b axis as before) and field plates are connected to vacuum electrical feedthroughs with coaxial cables. We used cryogenic SMA cables with stainless steel jackets to connect the mount assembly to the feedthrough in order to reduce the heat load on the crystal. With this setup, based on a roughly 16-hour spectral hole lifetime measured by Daniel Stedman, the crystal reaches temperatures below 5.6 K [38].

3.3.3 Static electric field plates

The measurement scheme involves resolving different orientations of ions by splitting spectral holes with small static electric fields. The necessary field magnitude is determined by the targeted spectral hole width of 100 kHz. In our initial experiments, however, we have so far only observed spectral holes that are broader than ~ 500 kHz, as explained in Section 4.2, so we need field plates that can split MHz-scale spectral holes. We apply electric fields across the D_1 axis of the crystal which has a linear Stark shift coefficient of 27.1 kHz/(V/cm) [42]. Therefore, to split 1 MHz spectral holes by > 2 MHz so that they can be clearly resolved, we require static electric fields greater than ~ 40 V/cm.

The experiment further requires that the electric field can be switched on and off quickly so that it does not limit the ~ 15 ms cycle time assumed in Section 2.3. With the ~ 3 mm plate separation of the crystal mount (Section 3.3.2), tens of volts must be applied to the cathode field plate to split MHz-scale holes. Since our arbitrary waveform generator (AWG) outputs only up to ± 2.5 V, we cannot directly use our AWG to apply voltages to the cathode field plate. But if we instead directly use a DC power supply, the response times would be too slow.
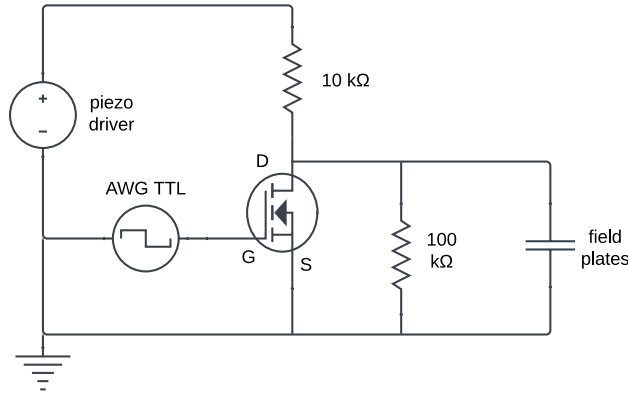

Figure 3.7: A schematic of the circuit used to quickly switch the voltage applied across the field plates.

To solve this issue, I built a simple circuit with an N-channel MOSFET, shown in Fig. 3.7. The applied voltage $V_{\text{app.}}$ is supplied by a piezo driver, which can output up to 100 V. A piezo driver is a good choice for this application since it is meant to drive capacitive loads, like our parallel field plates. With this circuit, by default, when $V_{\text{GS}} = 0$ V is applied to the MOSFET, D and S are open so that the driver applies a voltage $\frac{10}{11}V_{\text{app.}}$ across the field plates. When $V_{\text{GS}} > 2$ V is applied, D and S are shorted, so that 0 V is applied across the plates. Since the MOSFET has a fast response time, as shown in Fig. 3.8, we can then drive V_{GS} with our AWG to split MHz-scale spectral holes in sub-microsecond timescales.

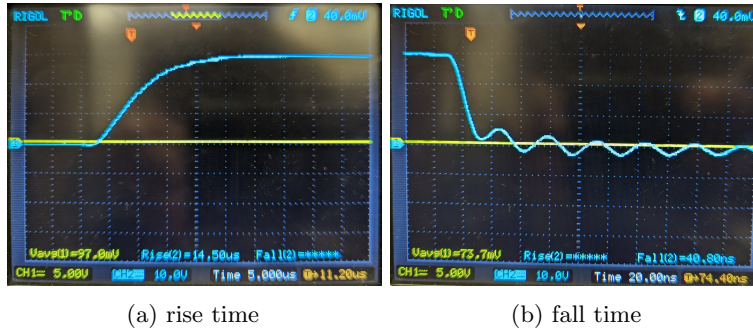(a) rise time   (b) fall time

Figure 3.8: The response of the switching circuit in Fig. 3.7, when a square pulse is applied to the MOSFET gate. The output voltage is measured in parallel with the field plates.

3.3.4   Resonant coil tuning

As described in Section 2.2, the measurement scheme involves direct rf spectroscopy between different hyperfine sublevels of the $^7F_0$ electronic state. As shown in Fig. 2.1, the relevant rf frequencies are 90, 119, and 209 MHz for the $\{b, \bar{b}\} \leftrightarrow \{c, \bar{c}\}$, $\{a, \bar{a}\} \leftrightarrow \{b, \bar{b}\}$, and $\{a, \bar{a}\} \leftrightarrow \{c, \bar{c}\}$ magnetic dipole transitions, respectively. One requirement on the rf magnetic field strength is that it translates to a Rabi frequency Ω that excites atoms on a faster timescale than the 15 ms coherence time. This corresponds to $\Omega \sim 70$ Hz, which is not a very stringent requirement.

More importantly, the number of ions involved in the rf spectroscopy, and thus the signal-to-noise of the measurement, is affected by the inhomogeneous linewidth $\Gamma_{\text{hfs,inhom.}}$ of the hyperfine transition that is driven. To efficiently excite an inhomogeneously broadened ensemble of atoms, power broadening $\Omega \gg \Gamma_{\text{hfs,inhom.}}$ or rapid adiabatic passage (RAP) [74] is required. A previous measurement has reported $\Gamma_{\text{hfs,inhom.}} \sim 70$ kHz on a $^7F_0$ hyperfine transition of ^{153}Eu [36]. Since the coherent quantum beats spectroscopy technique we describe in Section 2.4 works with RAP in certain parameter regimes [4], we estimate that it will relax the Ω requirement to ~ 5 kHz.

We observe that the matrix elements of the magnetic dipole operator for sublevels of $^7F_0$ – provided in Table A.1 – are almost all smaller than a nuclear magneton $\mu_n = 0.76$ kHz/G. To implement the measurement scheme, we then require magnetic field strengths greater than 10 G at radiofrequencies within a ~ 0.1 cm^3 scale volume. This presents somewhat of a technical challenge, demanding a resonating circuit and a compact in-vacuum cryogenic rf coil that does not dissipate too much heat. For this reason, version 2 of the crystal mount was designed around obtaining such fields. The following discussion focuses on my work tuning this rf coil to obtain strong magnetic fields. Details on the design of this coil and how it satisfies other technical requirements can be found in Julia Ford's MSc report [82].

Since inductive reactance $X = j2\pi f L$ increases with frequency f, it is easier to build resonant coils at lower frequencies. We select the 90 MHz $\{b, \bar{b}\} \leftrightarrow \{c, \bar{c}\}$ transition for our experiment for this reason. It is easier to obtain a strong magnetic field with a many-turn small-diameter coil wrapped around the crystal, but we still need to allow optical access along the b axis, as described in Section 3.3.2. As shown in Table A.1, this configuration corresponds to matrix elements of $|\langle|b\rangle|\vec{\mu}|c\rangle| = |\langle\bar{b}|\vec{\mu}|\bar{c}\rangle| = 0.403\,\mu_n$ and $|\langle|\bar{b}\rangle|\vec{\mu}|c\rangle| = |\langle b|\vec{\mu}|\bar{c}\rangle| = 0.354\,\mu_n$, translating to a ~ 16 G field for $\Omega \sim 5$ kHz.
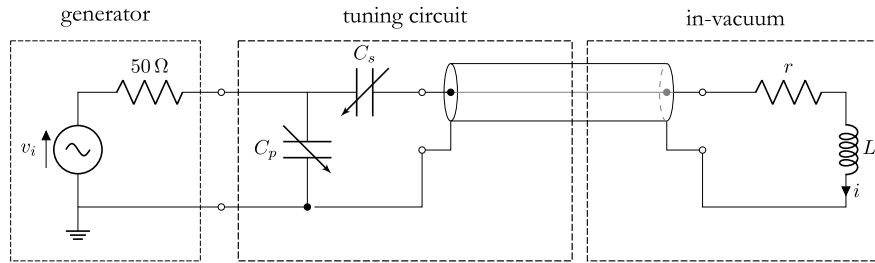

Figure 3.9: Diagram of the resonant circuit driving the rf magnetic field coil. As shown, the tuning circuit is connected to the coil through 50 Ω coaxial cables that act as transmission lines, partly out-of-vacuum and partly in-vacuum.

With the 20-turn, centimeter-scale coil that we implemented with the version 2 crystal mount, we expect magnetic fields on the order of 10 G for 1 A of current i through the coil. Currents in this range would also lead to a tolerable level of heat dissipation given the expected sub-100 milliOhm resistance r of the coil at cryogenic temperatures. We designed a resonant circuit, shown in Fig. 3.9, that we tune to deliver such currents to the rf coil using two out-of-vacuum, air-variable capacitors $(5 - 51$ pF): one in series (C_s) and one in parallel (C_p). Unlike the setups in other work [83], our resonant circuit does not require in-vacuum
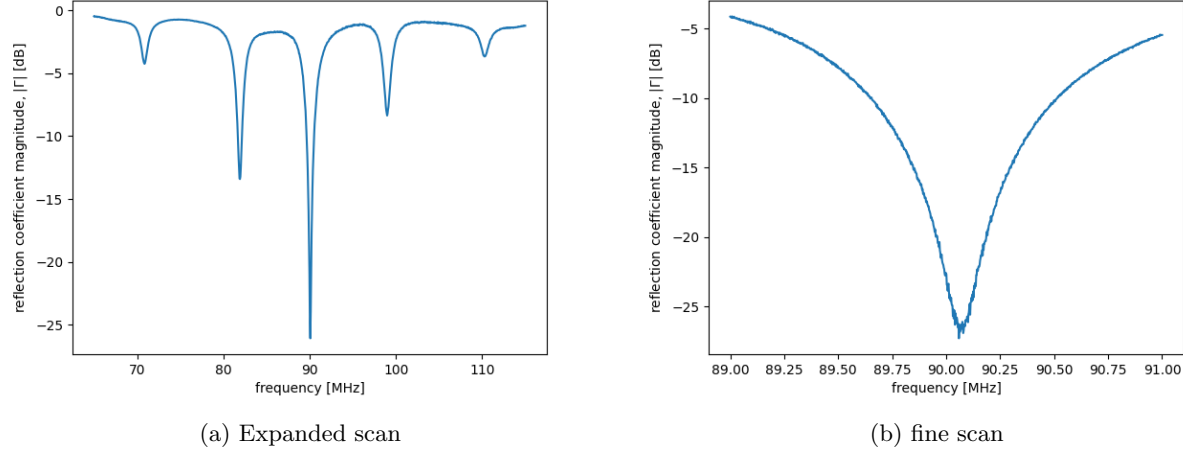
(a) Expanded scan

(b) fine scan

Figure 3.10: The single-port reflection spectra of the resonant coil circuit, after the capacitors were tuned to shift the resonance to 90 MHz. These measurements were made with a calibrated vector network analyzer. A broad scan is shown on the left and a fine scan is shown on the right.

capacitors and is less susceptible to changes due to cooldowns and warmups of the chamber because it uses in-vacuum coaxial cables that act as high-quality transmission lines at 90 MHz.

In order to obtain a coil resonance 90 MHz, we first connect an appropriate length (a few meters) of coaxial cable between the vacuum feedthrough for the coil and the capacitor tuning circuit. Since a 90 MHz signal corresponds to a ~ 2.2 m wavelength inside the cable, standing waves form within this length of cable which transforms the coil impedance as seen by the tuning circuit. By experimenting with cable lengths, we use this property to favorably transform the coil impedance before tuning the capacitors.

To tune the capacitors, we perform a single port reflection coefficient measurement using a vector network analyzer (VNA). The standing wave effect is evident in Fig. 3.10a, which shows a periodic coil resonance structure due to the wavelength of the signal and the length of the cable. As shown in Fig. 3.10b, the capacitors are tuned to obtain a large ($Q \sim 900$) coil resonance near 90.026 MHz (a more exact value for the $b \to c$ splitting). Given the 50 Ω impedance of our generator, this circuit would send ~ 2 A of current through the coil with only 0.5 W of rf power. The bandwidth of the resonance is ~ 100 kHz, which is well-matched to the $\Gamma_{\mathrm{hfs,inhom.}} \sim 70$ kHz frequency range over which the CQB technique with RAP will be applied. We also observed that the coil resonance is insensitive to mechanical disturbances of the tuning capacitors and that the resonance shifts by < 100 kHz during cooldowns and warmups. Altogether, this resonant coil system is robust and meets the technical requirements of the experiment.

3.3.5 Static magnetic field coils

The measurement scheme requires a static magnetic field in order the break the degeneracy between Kramers pairs. As an advantage of the CQB technique, it is possible to measure the splitting $\nu_{c\bar{c}}$ between c and $\bar{c}$ states by driving the $\{b, \bar{b}\} \leftrightarrow \{c, \bar{c}\}$ transitions even when spectral holes corresponding to each of the four transitions within this four-level subsystem are not separately resolved. For this reason, even with the small, sub-μ_n scale of the magnetic dipole matrix elements along the D_1 axis (Table A.1), the static magnetic field strength $\mathcal{B}_0$ requirements are not demanding.

A static magnetic field is still required for two reasons: (a) to serve as a bias field to reduce the effect of background field fluctuations on the measurement and (b) to measure a finite frequency $\nu_{c\bar{c}}$ with the CQB technique. In particular, we would like $\nu_{c\bar{c}}$ to be sufficiently large that at least one full fringe is mapped out

as the pulse separation T is swept between 0 and $T_2 = 15$ ms in the CQB sequence. This corresponds to a minimum $\nu_{c\bar{c}}$ of ~ 70 Hz, which is attained with $\mathcal{B}_0 \sim 2$ G. Julia Ford designed a pair of in-vacuum DC Helmholtz coils that achieves homogeneous static magnetic fields throughout the crystal volume up to $\mathcal{B}_0 \sim 10$ G with a ~ 1 A operating current. This coil has been assembled, but not yet installed in the apparatus.

3.4   Sequencing

The measurement scheme involves a complicated timing sequence, involving the control of multiple rf sidebands of the laser, a static electric field, and an rf magnetic field. The real sequences are more complicated than the schematic representation of Fig. 2.2; more detailed timing diagrams examples are shown in Figs. 4.2, 4.5, and 4.8. These sequences must be precisely timed with short dead times, as compared to the ~ 15 ms cycle time, in order to reach the projected sensitivity of the experiment.

Ideally, we would like one central piece of hardware to control any relevant experimental parameters that would change during one measurement cycle. Fig. 3.1 illustrates this with an arbitrary waveform generator (AWG) that sends signals to the many other devices in the experiment. In our early experiments, however, we ran sequences with M-Labs ARTIQ Sinara hardware: an FPGA system with rf synthesizer, TTL I/O, ADC, and DAC cards.

Eventually, with the Sinara, we ran into hardware limitations due to the frequency and amplitude modulation speeds of the synthesizers driving our AOMs. This limitation, along with the difficulty of low-level programming with ARTIQ and the inadequate buffered memory and sampling rate of the ADC card, led us to switch over to a Spectrum Instrumentation M4i-6622x8 AWG for our sequencing. This system is capable of running all of our current and expected future experimental sequences; it has three TTL output channels and four arbitrary voltage output channels with a sampling rate of 625 MHz and an output bandwidth of 200 MHz. We use 3 arbitrary output channels and 3 rf amplifiers to drive our AOMs and use the remaining arbitrary output to drive the rf coil. The signals from our two photodiodes are recorded on a 2-channel, 20-megahertz digitizer (Agilent L5432A), which is triggered by one of the TTL outputs of the AWG. An additional AWG TTL output is used to switch the static electric field on and off, as shown in Fig. 3.7.

Chapter 4

Experimental results

All of the individual measurement techniques contained in the ONIX scheme, outside of CQB spectroscopy, have been demonstrated in previous works. The novelty of the experiment lies in synthesizing these techniques to extract highly-sensitive $\mathcal{T}$-violating observables. Furthermore, the hardware described in Chapter 3 should meet all of the technical requirements of the experiment, although future upgrades will almost certainly be required for incremental improvements in statistics and adequate control of systematics. Therefore, in the following sections, I describe experimental results we obtained with our apparatus that demonstrate particular measurement techniques involved in the $\mathcal{T}$-violation scheme.

4.1 Absorption

As the first measurement on our experiment, we searched for the $^7F_0 \to {}^5D_0$ optical resonance of Eu^{3+} ions substituted for Y^{3+} ions in site 1 of YSO. To do this, we first broadly tune our laser to a vacuum wavelength of 580.04 nm, where previous authors observed the transition [51, 38]. We then locked our laser to our wavemeter and slowly adjusted the frequency setpoint over a ~ 10 GHz range until we discovered the resonance. We record the transmitted and incident light intensities using the two photodiodes in our detection setup. This first experiment was a continuous-wave (CW) measurement with ~ 1 mW of power that did not use the AOMs or the fast digitizer. Thus, this measurement was done at ~ 17 K to prevent spectral hole burning effects from distorting the lineshape.

Fig. 4.1 shows the optical depth we observe as a function of laser frequency, fitted to a Gaussian lineshape (parameters defined in the figure). The feature is centered at 516,847.624(2) GHz and consistent with the observations of other authors [51, 38]. The observed full-width at half-maximum (FWHM) inhomogeneous linewidth $\Gamma_{\mathrm{opt.,inhom.}} = 2\sqrt{2\ln 2}\sigma$ is 0.711(7) GHz and the observed peak absorption coefficient $\alpha_0 = A/d$ is 1.50(1) cm^{-1}, where $d = 1$ cm is the optical path length through the crystal. $\Gamma_{\mathrm{opt.,inhom.}}$ and α_0 are consistent with the trend observed in measurements of other crystals at different concentrations down to 0.02% [38, 84].

There is a visible asymmetry around the line center in Fig. 4.1, leading to a large reduced chi-squared $\chi^2_\nu = 26.7$ for our fit. We speculate that this occurred due to polarization drift during the measurement, which took ~ 20 minutes. As described in 3.2.2, the detection setup we use is sensitive to changes in polarization. Even so, this absorption measurement is adequate for our purposes since we are not interested in precision optical spectroscopy. Knowledge of the optical line center to 2 MHz is sufficient for us to pick the best spectral regions in which to burn holes.
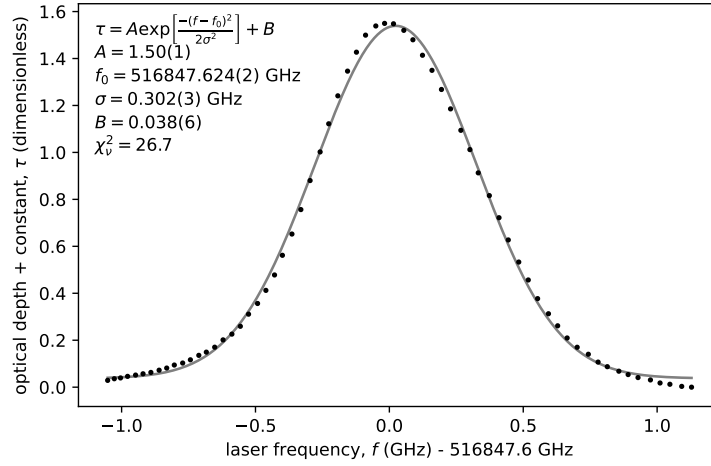
Figure 4.1: Absorption spectrum for the $^7F_0 \to {}^5D_0$ optical resonance of Eu^{3+} ions, substituted for Y^{3+} ions in site 1 of YSO. The solid line is a Gaussian fit to the data, with parameters defined in the top left.

4.2   Spectral hole burning

The next milestone in the experiment was burning spectral holes. Spectral hole-burning occurs through spontaneous decays in inhomogeneously-broadened ensembles with long-lived, but unresolved ground state sublevels. In Eu:YSO, an ion in a hyperfine sublevel $|i\rangle$ of $^7F_0$ can be optically excited to $^5D_0$ and then spontaneously decay to a *different* hyperfine sublevel $|j\rangle$. This can occur between an arbitrary pair of hyperfine states because of the broken symmetries in the crystal, as described in Section 2.1. Since imbalanced distributions of populations between $^7F_0$ hyperfine states are long-lived at low temperatures (T_1 in Section 3.3.1), prolonged or high intensity optical excitation at particular spectral regions within the inhomogeneous linewidth leads to *spectral holes*, where population has been depleted.
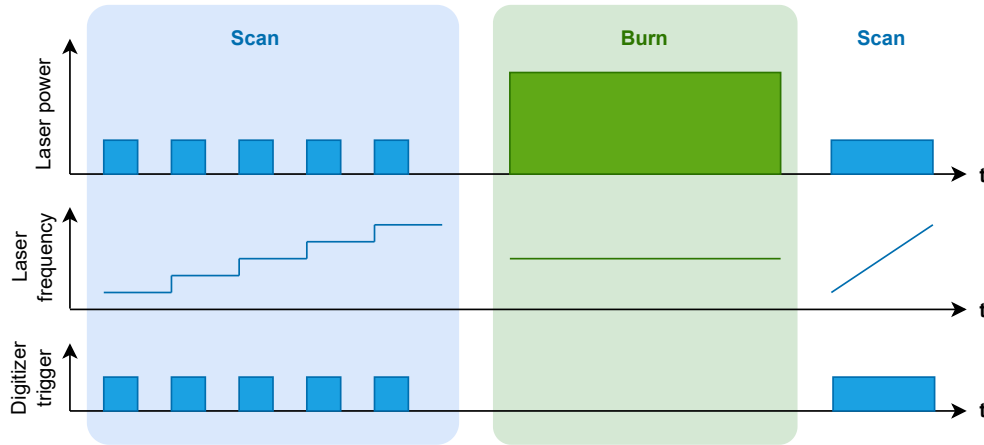

Figure 4.2: Schematic timing diagram for a spectral hole burning sequence, segmented into "scan" and "burn" phases. The scan phase on the right is represented in a simplified view, which is used in subsequent Figs. 4.5 and 4.8 as well.

To observe spectral holes, we implement the sequence represented in Fig. 4.2. The sequence has a "scan" phase and a "burn" phase, occurring in scan-burn-scan order. The scan phase is meant to read out the populations at different optical frequencies with minimum disturbance to the states of the atoms. Therefore, the scan involves low laser powers ($< 5\,\mu W$) and $< 500\,\mu s$ optical pulses with an AOM to prevent spectral

hole-burning from corrupting the readout. Using an AOM, we step the laser frequency and pulse the laser power once per frequency. Although not shown in Fig. 4.2, we repeat the entire scan phase $N_{\text{avg.}}$ times over the desired frequency range to obtain averaged results at each frequency. The burn phase involves shining the laser at high power ($> 500\,\mu\text{W}$) for > 100 ms at a fixed frequency to create a spectral hole. Thus, the first scan serves as a background measurement, in case spectral features already exist in the scan frequency range from previous experiments. The second scan records the spectrum after the burn. The background scan is then subtracted from the second scan to show the effect of the burn pulse.
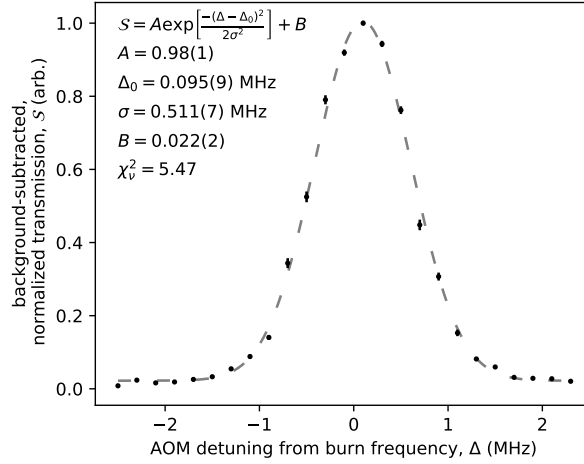

Figure 4.3: A spectral hole, produced from the sequence shown in Fig. 4.2. The solid line is a Gaussian fit to the data, with parameters defined in the top left.

Fig. 4.3 shows an example of a spectral hole, recorded with $N_{\text{avg.}} = 10$ and fitted to a Gaussian lineshape (parameters defined in the figure). There is a clear increase in transmission at the frequency of the burn pulse, corresponding to a depletion in the population at that frequency. The spectral hole FWHM linewidth of 2.41(3) MHz (after accounting for the factor of 2 from the double-passed AOM) is likely a result of the optical homogeneous linewidth. This measurement was done with the first crystal mount, which we believe cooled the crystal to 15 K, as described in Section 3.3.2. The two loop laser stabilization system, described in Section 3.1, was used for this measurement, so the laser linewidth of 10.1 kHz would have been much narrower than the spectral hole linewidth.

Notably, the fit in Fig. 4.3 shows a frequency shift of 0.19(2) MHz between the burn frequency and the center of the spectral hole, indicating that there may be laser frequency fluctuations or drifts in our system. Furthermore, even with the second version of our crystal mount, we are unable to burn spectral holes narrower than ~ 500 kHz. With this mount, we have observed spectral hole lifetimes consistent with temperatures below 5.6 K, which should correspond to a sub-kilohertz optical inhomogeneous linewidth [38]. This is a puzzle that is currently unsolved.

As another milestone in the experiment, we observed a spectral *antihole*, as shown in Fig. 4.4. Antiholes occur because the population depleted due to a spectral hole must be redistributed to different $^7F_0$ hyperfine states, leading to excess population detuned from the spectral hole by certain linear combinations of the $^7F_0$ and $^5D_0$ hyperfine splittings (more detail in Section 4.4). The population from one spectral hole can be redistributed to many antiholes (see Fig. 4.7), so an antihole will always be much smaller than the main spectral hole. In Fig. 4.4, we use the wide bandwidth of our double-pass AOM to capture both a hole and antihole in a scan of one AOM, using a scan frequency-shifted modification to the sequence presented in Fig. 4.2. The background level in the figure does not reach zero because of spectral hole-burning effects during the scan phase.
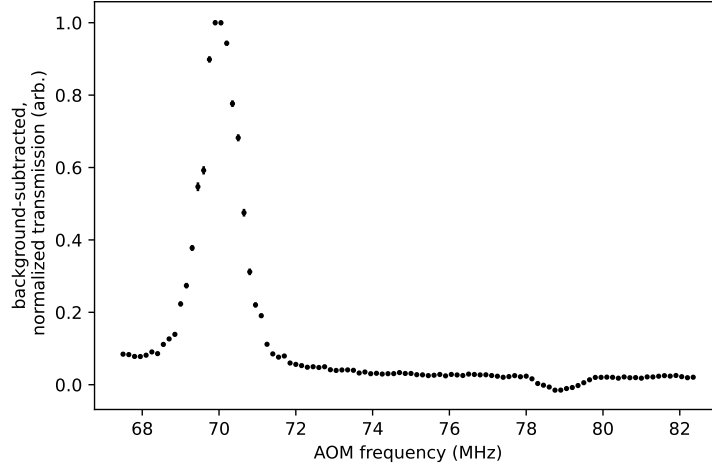
Figure 4.4: A spectral antihole paired with its corresponding primary spectral hole.

4.3   Orientation-resolved splittings of spectral holes

Our $\mathcal{T}$-violation measurement scheme crucially involves resolving different orientations of ions within the lattice, using the observed linear Stark shift of spectral holes in this system under applied electric fields in the lab [42].
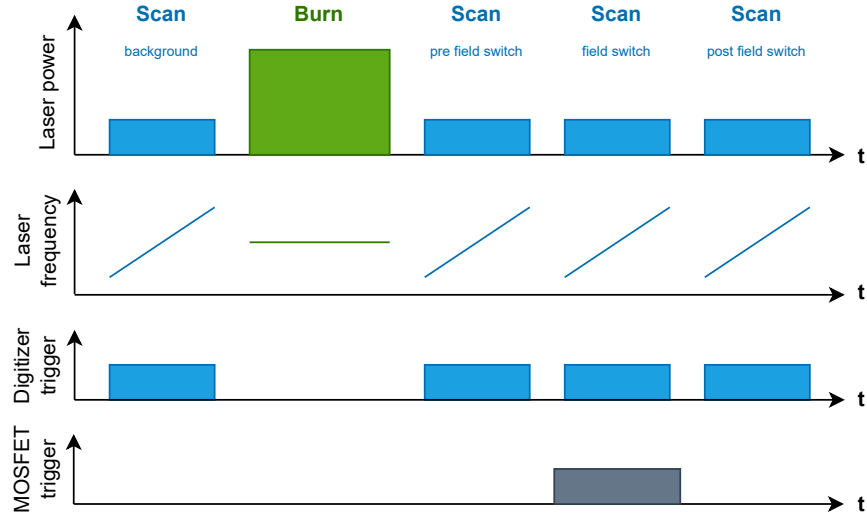

Figure 4.5: Schematic timing diagram for a spectral hole splitting sequence. The sequence uses the field switching circuit described in Section 3.3.3.

To demonstrate this important technique, we implement the sequence shown in Fig. 4.5, a simple modification to the sequence in Fig. 4.2 that adds additional scan phases and a switch of the electric field using the circuit described in Section 3.3.3. Before running the sequence, the piezo driver outputs a fixed voltage. By default, when the MOSFET gate signal is low, the field-switching circuit applies the voltage to the field plates, so an electric field is applied before holes are burned in this sequence. During one of the scans in the sequence, the circuit switches off the field applied to the crystal. This process of burning a hole in the presence of an electric field and then turning off the field leads to same spectral hole splitting effect as burning a hole without a field and then turning it on. In both cases, differently-oriented ions are in different

spectral classes within the inhomogeneous distribution, and switching the field on or off shifts their position within the optical spectrum.
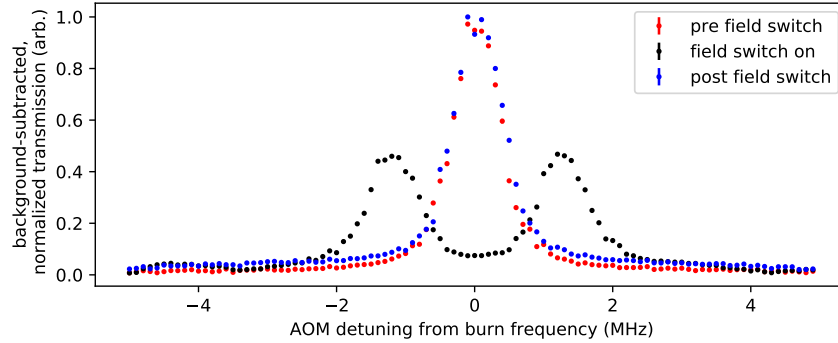

Figure 4.6: Overlaid spectra showing a spectral hole splitting when 30 V applied to the electric field plates is turned on and off. This data was produced using the sequence shown in Fig. 4.5.

Fig. 4.6 shows the splitting of a spectral hole due to a 30 V applied voltage, controlled by the switching circuit. The data from the background scan phase before the burn is subtracted from each of the three scan phases that occur after the burn. It is evident that the spectral hole splits into two holes of roughly equal height when the field is switched and becomes a single hole again once the field is restored. There are some ripples specifically in the field-switched scan because the background subtraction is imperfect; other, pre-existing spectral features outside of the scan frequency range can be shifted into view by the field switch. The pre-field switch and post-field switch data do not exactly overlap due to the finite spectral hole lifetime and because of spectral hole-burning effects during the scan.

4.4   Hyperfine state preparation

As shown in Fig. 3.4, in order to prepare ions in a given spectral region into a particular $^7F_0$ Kramers pair, our experiment uses the frequency shifts from three AOMs to each address different combinations of Kramers pairs on the $^7F_0 \to {}^5D_0$ transition. Here, we explain why these three laser frequencies are required.

In Eu:YSO, the inhomogeneous linewidth of the $^7F_0 \to^5 D_0$ optical transition (~ 700 MHz, as in Fig. 4.1) obscures the the hyperfine structure of the $^7F_0$ and $^5D_0$ states (~ 200 MHz and ~ 450 MHz, as in Fig. 3.4). For this reason, spectral hole burning with a single laser frequency ν does not address a particular transition from $^7F_0$ hyperfine sublevel $|i\rangle$ to $^5D_0$ hyperfine sublevel $|j\rangle$. Rather, it addresses an average of all possible transitions, with relative probabilities given in Table 2.1.

Single-frequency spectral hole-burning can lead to complicated (anti)hole spectra. In zero field, there are three Kramers pairs in $^7F_0$ and three in $^5D_0$, as shown in Fig. 3.4, leading to nine possible nondegenerate combinations of $|i\rangle$ and $|j\rangle$. The hole burning laser frequency simultaneously addresses all nine of these combinations, so we consider the possibilities one by one. If we assume that ν addresses a particular transition $|i\rangle \to |j\rangle$ with relative strength A_{ij}, relaxation from $^5D_0$ will take $|j\rangle$ to a $^7F_0$ hyperfine sublevel $|k\rangle$, not necessarily $|i\rangle$. $^5D_0$ relaxes into $^7F_0$ via spontaneous photon emission into ^7F_J (primarily $^7F_1$) followed by phonon emission [38]. Prediction of the relative $|j\rangle \to |k\rangle$ branching ratios is thus complicated, so we assume that all the $|j\rangle \to |k\rangle$ have equal branching ratios for simplicity in this discussion. The redistributed population from $|j\rangle \to |k\rangle$ creates (anti)holes in the optical spectrum that are detuned from ν by Δ_{ijkl} due to the transitions $|k\rangle \to |l\rangle$. The relative sizes of those (anti)holes will then be $A_{ij}A_{kl}$. All features where $i = k$ will be holes, while the others will be antiholes.
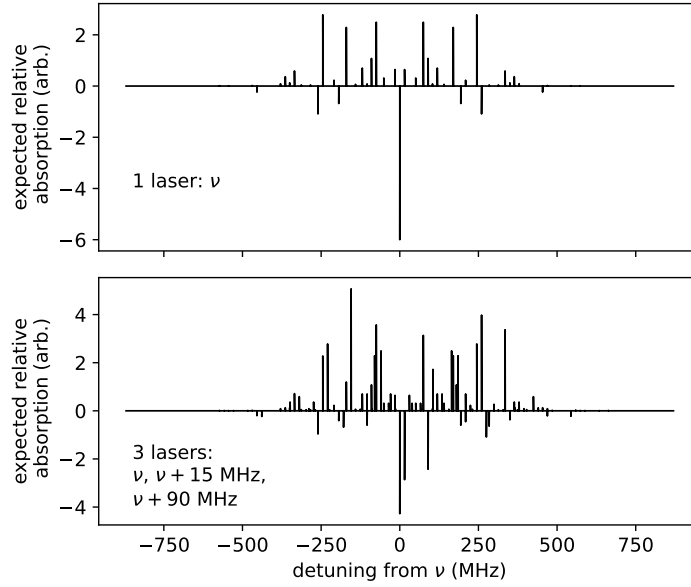
Figure 4.7: Calculations showing the detunings and magnitudes of holes and antiholes arising from spectral hole burning with one (top) and three (bottom) laser frequencies. The details of the calculation are explained in the text.

The top spectrum in Fig. 4.7 plots negative (positive) delta functions of magnitude $A_{ij}A_{kl}$ and offset Δ_{ijkl} to represent all 81 possible holes (antiholes) that arise from all $\{i, j, k, l\}$ combinations due to spectral burning at ω_0. Some of these 81 features are degenerate, so their $A_{ij}A_{kl}$ are summed together, leading to 49 unique features including the central hole.

To allow for hyperfine state preparation within this complicated system, three laser frequencies are chosen with relative detunings that address all three $^7F_0$ states and at least two $^5D_0$ states [40], as in Fig. 3.4. In doing so, for a particular, "selected" spectral class of atoms, each $^7F_0$ hyperfine state will be resonant with one of the three laser frequencies. In other, "unselected" spectral classes, two or fewer hyperfine states will be resonant with one of the laser frequencies because, say, the AOM meant to address $c \to b$ in Fig. 3.4 instead addresses $b \to a$. Optical pumping will eventually drive these unselected spectral classes into hyperfine states that are dark to the laser. The leftover population – purely from the selected spectral class – at the optical burn frequencies of $\nu = \nu_0 + 145$ MHz, $\nu_0 + 160$ MHz, and $\nu_0 + 235$ MHz will be purely in $^7F_0$ states $\{c, \bar{c}\}$, $\{a, \bar{a}\}$, and $\{b, \bar{b}\}$, respectively. The bottom spectrum in Fig. 4.7 shows the (anti)hole structure for the three listed laser frequencies, generated by shifting three single-frequency spectra by the appropriate detunings and summing them together. There are $109 < 3 \times 49$ unique features because of further degeneracies. Note that saturation effects are neglected by this method of calculation.

To implement hyperfine state preparation, we apply the two-stage sequence shown in Fig. 4.8. The "class cleaning" stage in our state preparation sequence involves burning "spectral chasms". A spectral chasm is essentially a broad spectral hole that we burn by sweeping the laser frequency while the laser is on at high power. This leads to a wider spectral hole than is attainable purely from the laser linewidth or power broadening. The main function of a spectral chasm is to reset a given spectral region by saturating and thus flattening it so that features from previous experiments do not influence the current experiment. Three spectral chasms are burned with the three AOMs during the class cleaning stage to clearly resolve the three $^7F_0$ Kramers pairs for the selected spectral classes.

The spectral chasms at all three spectral regions after class cleaning are shown in red in Fig. 4.9. As expected, the chasms are quite flat. The minor slopes in the chasms likely occur due to the bandwidth of
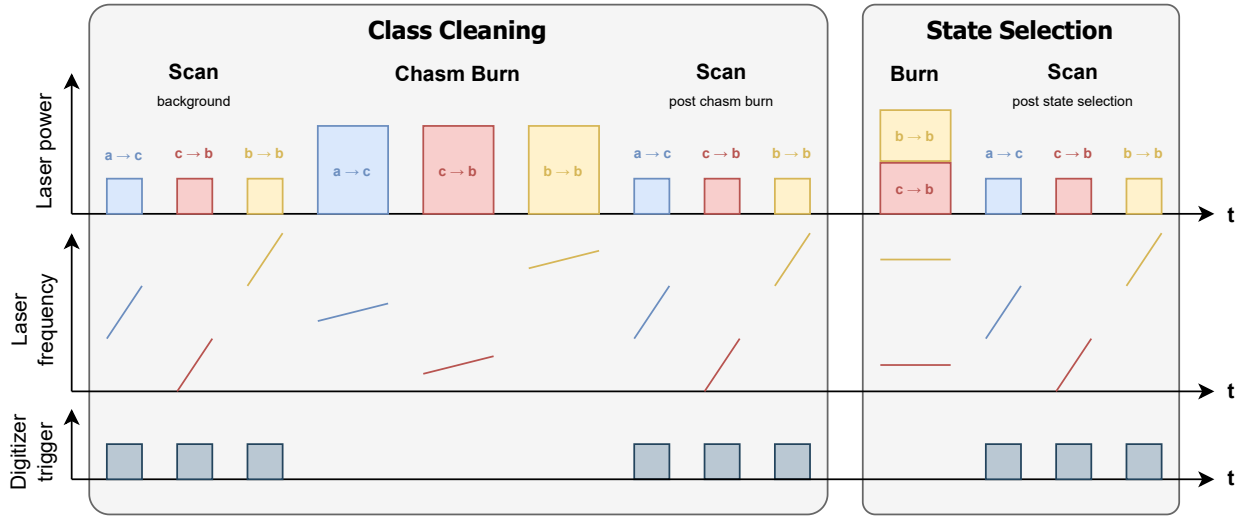
Figure 4.8: Schematic timing diagram for hyperfine state preparation. The sequence uses three AOMs to address transitions between different pairs of $^7F_0 \to {}^5D_0$ hyperfine sublevels, assigned as 160 MHz for $a \to c$, 145 MHz for $c \to b$, and 235 MHz for $b \to b$, as per Fig. 3.1.

the AOMs. Although the recorded spectra from scan phases are normalized by incident power, the incident power on the crystal during a chasm burn phase varies as a function of frequency. Feedforward control will be implemented to mitigate this effect.
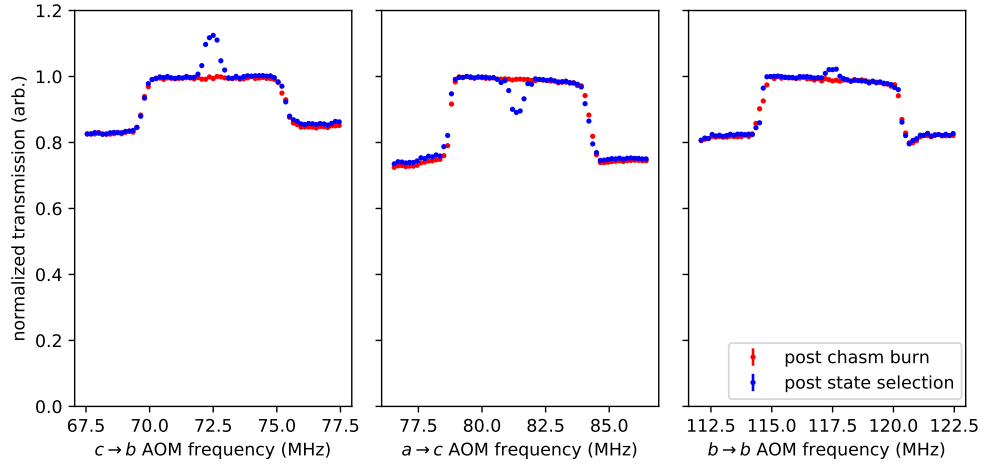

Figure 4.9: Overlaid spectra showing spectral chasms created by the three AOMs after class cleaning, along with the holes or antiholes created within those chasms by subsequent state selection into $a, \bar{a}$. Note that the normalization applied to the y-axis is different for each AOM.

The state selection stage of Fig. 4.8 involves burning a smaller hole or antihole within the spectral chasms prepared by class cleaning. This is done by simultaneously burning with two of the three AOMs while their frequencies are fixed such that they are offset by a $^7F_0 \to {}^5D_0$ hyperfine splitting. In the example sequence, the $c \to b$ and $b \to b$ AOMs are on during the state selection, optically pumping population into the $a, \bar{a}$ sublevels. The results are shown in blue in Fig. 4.9. As expected, there are holes within the spectral chasms in $c \to b$ and $b \to b$, where population has been depleted to fill an antihole within the spectral chasm in $a \to c$. Note that the relative transition probabilities are different for the three transitions (see Table 2.1), so direct comparison of spectral (anti)hole heights is not meaningful.

To obtain higher-quality spectral features, we are currently experimenting with more complicated versions of the state preparation sequence shown in Fig. 4.8. For instance, it may help to repeat the chasm burn phase several times, so that e.g. atoms that are excited via $a \to c$ and then decay back into a are re-excited by a subsequent $a \to c$ chasm burn rather than left behind. This should result in higher state purities in each of the spectral chasms, even if the total chasm burn phase is the same length as it was with one repetition. The power balance between the three AOMs is also currently unexplored in our sequences, which use roughly equal power in all three beams, but could lead to more efficient state preparation if adjusted to compensate for the relative transition probabilities.

4.5 Measurement of the differential electric dipole moment

As a test of our apparatus as compared to the literature, we measured the differential electric dipole moment $\Delta \vec{D} \equiv 2\Delta\alpha \, \vec{\mathcal{E}}_{\text{xtl}}$ (parameters defined in Sections 2.1 and 2.3) of the $^{7}F_0 \to {}^{5}D_0$ transition. $\Delta \vec{D}$ causes linear Stark splittings $\Delta\nu_E = \Delta\vec{D} \cdot \vec{\mathcal{E}}_{\text{lab}}$ of spectral holes when electric fields $\vec{\mathcal{E}}_{\text{lab}}$ are applied in the lab. So a measurement of ΔD amounts to measuring the spectral hole splittings as $\mathcal{E}_{\text{lab}}$ is varied.

(a) $V_{\text{app.}} = 30$ V
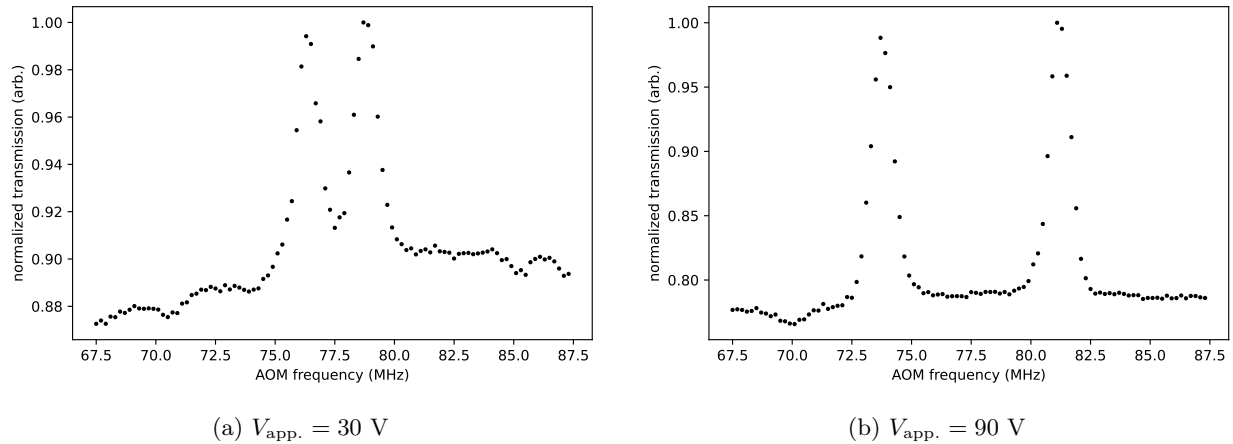
(b) $V_{\text{app.}} = 90$ V

Figure 4.10: Spectral hole splittings when two different voltages applied to the electric field plates are switched. $V_{\text{app.}}$ is the voltage output of the piezo driver in the circuit of Fig. 3.7. Note that background subtraction is not applied to these two plots.

To obtain spectral hole splittings over a range of $\mathcal{E}_{\text{lab}}$ values, we vary the voltage output $V_{\text{app.}}$ of the piezo driver in the circuit shown in Fig. 3.7. We obtain measurements over a range of $25 \, \text{V} \leq V_{\text{app.}} \leq 90 \, \text{V}$ in steps of 5 V. Each measurement was made with a new spectral hole burned at a different optical frequency, which affects the spectral hole depths but should not affect $\Delta\vec{D}$. Two example spectra, obtained with $N_{\text{avg}} = 10$, are shown in Fig. 4.10. Although the simplest way to extract spectral hole splittings would be to fit a sum of two Gaussians to each of these spectra, this method would be sensitive to the asymmetries of our observed holes due to any imperfections in the burn phase and the possibility that they are non-Gaussian. In many cases, our spectral hole lineshapes are not as Gaussian as the example in Fig. 4.3.

Instead, we take numerical derivatives of our hole spectra and use the zero-crossings to identify spectral hole centers. We do this by initially fitting the spectrum to a sum of two Gaussians and using the fitted hole centers to select a small region around both spectral holes. Within these small regions, we take the numerical derivative and find the zero-crossing points with linear fits. The detunings Δf between the fitted zero crossings provide the spectral hole splittings for our measurement of ΔD.

In Fig. 4.11, we plot all our fitted Δf values as a function of the applied voltage $V_{\text{xtl}} = \frac{10}{11}V_{\text{app.}}$ across the crystal, accounting for the voltage division by the MOSFET circuit (Fig. 3.7) and verified by a precision
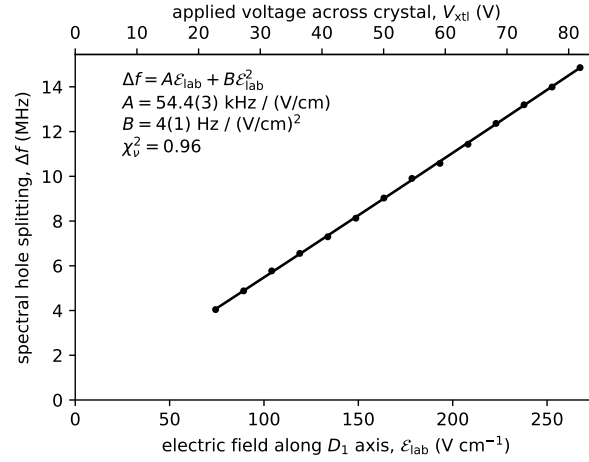
Figure 4.11: Fitted spectral hole splittings Δf as a function of the applied electric field $\mathcal{E}_{\text{lab}}$ across the D_1 axis of the crystal. The splittings are fit to a sum of linear and quadratic functions, with parameters defined in the top left. Uncertainties in Δf and the applied voltage V_{xtl} are too small to be visible in the figure. The $\mathcal{E}_{\text{lab}}$ uncertainty is larger but it is not plotted, as it originates from a systematic as described in the text.

multimeter. The secondary x-axis is the resulting electric field $\mathcal{E}_{\text{lab}} = V_{\text{xtl}}/d$ across the D_1 axis of the crystal, accounting for the field plate separation $d = 3.06(3)$ mm. The uncertainty in d is not included in the plot.

We fit our Δf data to a sum of linear and quadratic terms in $\mathcal{E}_{\text{lab}}$, as shown in the top left of Fig. 4.11. The fitted differential electric dipole moment is $\Delta D = A/2 = 27.2 \pm 0.2$ (stat.) ± 0.3 (sys.) kHz / (V/cm) where the systematic uncertainty comes from the uncertainty in d. The data is extremely linear, as indicated by the reduced chi-squared of $\chi^2_\nu = 0.96$ and the small quadratic coefficient $B = 4(1)$ Hz / (V/cm)^2. This agrees extremely well with the literature value of $\Delta D_{\text{lit.}} = 27.18 \pm 0.05$ (stat.) ± 0.2 (sys.) kHz / (V/cm) [42].

A possible systematic error comes from the true orientation of the crystal dielectric axes relative to the applied electric field axis. It is unlikely that the field plates were epoxied flush to the $D_2 - b$ faces of the crystal since the epoxying process was not done in a precision mount. This is also why the uncertainty in d is large, as it was backed out from images of the crystal in the mount. Further, the crystal itself may not have been cut exactly along its dielectric axes by the grower (Teledyne FLIR). The latter was the largest systematic error in the measurements of Ref. [42]. Although it is difficult to quantify these two misalignments, this measurement demonstrates the capabilities of our apparatus. The precise value of ΔD is not important to our experiment: $\Delta \nu_E$ need only be large enough that different orientations of ions are separately resolved.

Chapter 5

Summary & Outlook

In this report, I introduced a means to measure $\mathcal{T}$-violation with improved sensitivity, using octupole-deformed nuclei doped into non-centrosymmetric sites in a crystal. Our approach leverages the high intrinsic T-violation sensitivity of octupole-deformed nuclei, while using electrically polarized ions that are deeply trapped within a crystal. In order to match the enhanced precision available in this system with the required level of systematic error control, we have identified a number of tests and reversals to isolate genuine new physics from spurious backgrounds. Although a low symmetry solid-state system may seem to be a complex place for precision measurements, we have shown how the unique properties of Eu:YSO paired with an appropriate measurement scheme can yield high sensitivity to T-violation.

Our $\mathcal{T}$-violation measurement can be performed using a simple and compact experimental system. This report presented the apparatus we are developing to realize this measurement and verified its capabilities with high-quality experimental data. The techniques that we demonstrated – spectral hole burning, Stark splittings of holes, and hyperfine state preparation – serve as important milestones towards implementing the full measurement sequence.

In the near future, we plan to directly drive the $^7F_0$ hyperfine $b \rightarrow c$ transitions with our resonant rf coil, after preparing our atoms in $b, \bar{b}$ using our state preparation sequence. We will then perform rf spectroscopy, reading out populations by comparing spectral (anti)hole heights on the $b \rightarrow b$ and $c \rightarrow b$ optical transitions before and after the rf pulses. Once the rf is functional, we will install the static magnetic field coils that we have assembled into our chamber, providing a bias field that breaks the $b, \bar{b}$ and $c, \bar{c}$ degeneracies. At that point, we will have all the technical capabilities in place for our $\mathcal{T}$-violation measurement scheme. The main concerns would then be optimizing our measurements so that they are shot-noise-limited and characterizing systematic effects in our apparatus.

As a separate path, we may explore *optical* CQB measurements soon. This would first involve preparing our atoms in $c, \bar{c}$ and then applying a small static magnetic field to break Kramers degeneracies. We could then measure the $c - \bar{c}$ splitting by driving $c, \bar{c}$ to any of the $^5D_0$ hyperfine Kramers pairs, with two π-pulses and a pulse separation as in CQB. Although the coherence time may be limited to the 2 ms optical lifetime [38] in this scheme, it would be interesting as a first experimental demonstration of the CQB technique and as a backup option for our $\mathcal{T}$-violation scheme in case of technical complications with the rf coil.

In summary, during this MSc degree, we have developed a novel and promising nuclear $\mathcal{T}$-violation scheme and made major inroads towards realizing the experiment. The unique properties and previous studies of the Eu:YSO system have allowed us to build a precision measurement that could very soon test new physics at the PeV-scale.

Appendix A

Matrix elements of the magnetic dipole moment operator

This section summarizes the matrix elements of the magnetic dipole moment operator in the $^7F_0$ state of $^{153}\text{Eu}^{3+}$ in YSO, along the three crystallographic axes of the host crystal.

	$|a\rangle$	$|\bar{a}\rangle$	$|b\rangle$	$|\bar{b}\rangle$	$|c\rangle$	$|\bar{c}\rangle$
$\langle a|$	0.746	0.021	0.218	0.109	0.054	0.050
$\langle \bar{a}|$	0.021	0.746	0.109	0.218	0.050	0.054
$\langle b|$	0.218	0.109	0.351	0.220	0.299	0.167
$\langle \bar{b}|$	0.109	0.218	0.220	0.351	0.167	0.299
$\langle c|$	0.054	0.050	0.299	0.167	0.025	0.110
$\langle \bar{c}|$	0.050	0.054	0.167	0.299	0.110	0.025

(a) D_1 axis

	$|a\rangle$	$|\bar{a}\rangle$	$|b\rangle$	$|\bar{b}\rangle$	$|c\rangle$	$|\bar{c}\rangle$
$\langle a|$	0.487	0.020	0.231	0.040	0.056	0.027
$\langle \bar{a}|$	0.020	0.487	0.040	0.231	0.027	0.056
$\langle b|$	0.231	0.040	0.248	0.198	0.247	0.039
$\langle \bar{b}|$	0.040	0.231	0.198	0.248	0.039	0.247
$\langle c|$	0.056	0.027	0.247	0.039	0.436	0.091
$\langle \bar{c}|$	0.027	0.056	0.039	0.247	0.091	0.436

(b) D_2 axis

	$|a\rangle$	$|\bar{a}\rangle$	$|b\rangle$	$|\bar{b}\rangle$	$|c\rangle$	$|\bar{c}\rangle$
$\langle a|$	0.199	0.040	0.568	0.188	0.098	0.089
$\langle \bar{a}|$	0.040	0.199	0.188	0.568	0.089	0.098
$\langle b|$	0.568	0.188	0.402	0.367	0.403	0.354
$\langle \bar{b}|$	0.188	0.568	0.367	0.402	0.354	0.403
$\langle c|$	0.098	0.089	0.403	0.354	1.169	0.123
$\langle \bar{c}|$	0.089	0.098	0.354	0.403	0.123	1.169

(c) b axis

Table A.1: Matrix element magnitudes $|\langle j|\vec{\mu}|i\rangle|$ of the magnetic dipole operator $\vec{\mu} = \mathbf{M} \cdot \vec{I}$ along the three crystallographic axes in units of the nuclear magneton μ_n. j and i denote hyperfine sublevels in the $^7F_0$ state of $^{153}\text{Eu}^{3+}$ in YSO in zero magnetic field. These values were calculated using the constants measured in Refs. [51, 48], adjusted as described in Section 2.1.

Bibliography

[1] H. D. Ramachandran and A. C. Vutha, "Nuclear T-violation search using octupolar nuclei in a crystal," in The 27th International Conference on Atomic Physics (2022).

[2] H. D. Ramachandran and A. C. Vutha, Phys. Rev. A **108**, 012819 (2023).

[3] S. J. Li, H. D. Ramachandran, R. Anderson, and A. C. Vutha, New J. Phys **25**, 082001 (2023).

[4] H. D. Ramachandran, J. E. Ford, and A. C. Vutha, "Coherent quantum beats: spectroscopy of energy differences masked by inhomogeneous broadening," (2023), arXiv:2304.06189 [physics.atom-ph].

[5] A. D. Sakharov, Sov. Phys. Uspekhi **34**, 392 (1991).

[6] M. B. Gavela, P. Hernandez, J. Orloff, and O. Pene, Mod. Phys. Lett. A **9**, 795 (1994), arXiv:hep-ph/9312215.

[7] P. Huet and E. Sather, Phys. Rev. D **51**, 379 (1995).

[8] K. Abe *et al.* (T2K), Nature **580**, 339 (2020), [Erratum: Nature 583, E16 (2020)].

[9] R. Crewther, P. Di Vecchia, G. Veneziano, and E. Witten, Physics Letters B **88**, 123 (1979).

[10] B. Graner, Y. Chen, E. G. Lindahl, and B. R. Heckel, Phys. Rev. Lett. **116**, 161601 (2016).

[11] D. DeMille, J. M. Doyle, and A. O. Sushkov, Science **357**, 990 (2017).

[12] J. Engel, M. J. Ramsey-Musolf, and U. van Kolck, Progress in Particle and Nuclear Physics **71**, 21 (2013).

[13] H. M. Gray, Reviews in Physics **6**, 100053 (2021).

[14] R. Alarcon *et al.*, in *Snowmass 2021: Fundamental physics in small experiments* (2022) arXiv:2203.08103 [hep-ph].

[15] Y. Ema, T. Gao, and M. Pospelov, Phys. Rev. Lett. **129**, 231801 (2022).

[16] Y. Yamaguchi and N. Yamanaka, Phys. Rev. D **103**, 013001 (2021).

[17] M. Pospelov and A. Ritz, Annals of Physics **318**, 119 (2005).

[18] O. P. Sushkov, V. V. Flambaum, and I. B. Khriplovich, Sov. Phys. - JETP **60** (1984).

[19] L. I. Schiff, Phys. Rev. **132**, 2194 (1963).

[20] V. V. Flambaum and A. Kozlov, Phys. Rev. A **85**, 022505 (2012).

[21] L. V. Skripnikov, N. S. Mosyagin, A. V. Titov, and V. V. Flambaum, Phys. Chem. Chem. Phys. **22**, 18374 (2020).

[22] V. V. Flambaum and A. J. Mansour, Phys. Rev. C **105**, 065503 (2022).

[23] P. G. H. Sandars, Phys. Rev. Lett. **19**, 1396 (1967).

[24] D. A. Wilkening, N. F. Ramsey, and D. J. Larson, Phys. Rev. A **29**, 425 (1984).

[25] T. A. Isaev, S. Hoekstra, and R. Berger, Phys. Rev. A **82**, 052521 (2010).

[26] J. O. Grasdijk, O. Timgren, J. Kastelic, T. Wright, S. K. Lamoreaux, D. P. DeMille, K. Wenz, M. Aitken, T. Zelevinsky, T. Winick, *et al.*, Quantum Science and Technology **6**, 044007 (2021).

[27] T. Fleig and D. DeMille, New Journal of Physics **23**, 113039 (2021).

[28] M. Fan, C. A. Holliman, X. Shi, H. Zhang, M. W. Straus, X. Li, S. W. Buechele, and A. M. Jayich, Phys. Rev. Lett. **126**, 023002 (2021).

[29] J. Kłos, H. Li, E. Tiesinga, and S. Kotochigova, New Journal of Physics **24**, 025005 (2022).

[30] P. Yu and N. R. Hutzler, Phys. Rev. Lett. **126**, 023003 (2021).

[31] J. T. Singh, Hyperfine Interact. **240**, 29 (2019).

[32] V. V. Flambaum and V. A. Dzuba, Phys. Rev. A **101**, 1 (2020).

[33] V. V. Flambaum and H. Feldmeier, Phys. Rev. C **101**, 1 (2020).

[34] A. Mirzai, A. Ahadi, S. Melin, and P. Olsson, Mech. Mater. **154**, 103739 (2021).

[35] M. Zhong, M. P. Hedges, R. L. Ahlefeldt, J. G. Bartholomew, S. E. Beavan, S. M. Wittig, J. J. Longdell, and M. J. Sellars, Nature **517**, 177 (2015).

[36] N. Timoney, B. Lauritzen, I. Usmani, M. Afzelius, and N. Gisin, J. Phys. B: At. Mol. Opt. Phys. **45**, 124001 (2012).

[37] T. Zhong and P. Goldner, Nanophotonics **8**, 2003 (2019).

[38] F. Könz, Y. Sun, C. W. Thiel, R. L. Cone, R. W. Equall, R. L. Hutcheson, and R. M. Macfarlane, Phys. Rev. B **68**, 085109 (2003).

[39] E. Z. Cruzeiro, J. Etesse, A. Tiranov, P.-A. Bourdel, F. Fröwis, P. Goldner, N. Gisin, and M. Afzelius, Phys. Rev. B **97**, 094416 (2018).

[40] B. Lauritzen, N. Timoney, N. Gisin, M. Afzelius, H. de Riedmatten, Y. Sun, R. M. Macfarlane, and R. L. Cone, Phys. Rev. B **85**, 115111 (2012).

[41] A. Arcangeli, R. M. Macfarlane, A. Ferrier, and P. Goldner, Phys. Rev. B **92**, 224401 (2015).

[42] S. Zhang, N. Lučić, N. Galland, R. Le Targat, P. Goldner, B. Fang, S. Seidelin, and Y. Le Coq, Appl. Phys. Lett. **117**, 221102 (2020).

[43] A. Kaplyanskii and R. McFarlane, *Spectroscopy of Crystals Containing Rare Earth Ions* (Elsevier, 2012).

[44] A. W. Overhauser and H. Rüchardt, Phys. Rev. **112**, 722 (1958).

[45] W. Kaiser, S. Sugano, and D. L. Wood, Phys. Rev. Lett. **6**, 605 (1961).

[46] A. Kaplyanskii, J. Luminescence **100**, 21 (2002).

[47] K. M. Smith, M. F. Reid, M. J. Sellars, and R. L. Ahlefeldt, Phys. Rev. B **105**, 125141 (2022).

[48] J. J. Longdell, A. L. Alexander, and M. J. Sellars, Phys. Rev. B **74**, 195101 (2006).

[49] N. Stone, At. Data Nucl. Data Tables **90**, 75 (2005).

[50] M. J. Klein, Am. J. Phys. **20**, 65 (1952).

[51] R. Yano, M. Mitsunaga, and N. Uesugi, Opt. Lett. **16**, 1884 (1991).

[52] R. Yano, M. Mitsunaga, and N. Uesugi, J. Opt. Soc. Am. B **9**, 992 (1992).

[53] R. Macfarlane and R. Shelby, in *Modern Problems in Condensed Matter Sciences*, Vol. 21 (Elsevier, 1987) pp. 51–184.

[54] R. Macfarlane, A. Arcangeli, A. Ferrier, and P. Goldner, Phys. Rev. Lett. **113**, 157603 (2014).

[55] A. Arcangeli, M. Lovrić, B. Tumino, A. Ferrier, and P. Goldner, Phys. Rev. B **89**, 184305 (2014).

[56] D. DeMille, F. Bay, S. Bickman, D. Kawall, D. Krause Jr, S. Maxwell, and L. Hunter, Phys. Rev. A **61**, 052507 (2000).

[57] N. C. Carvalho, J.-M. Le Floch, J. Krupka, and M. Tobar, Appl. Phys. Lett. **106** (2015), 10.1063/1.4920987.

[58] C. Clavaguéra and J. Dognon, Chem. Phys. **311**, 169 (2005).

[59] G. Nishimura, M. Tanaka, A. Kurita, and T. Kushida, J. Luminescence **48**, 473 (1991).

[60] V. V. Flambaum, Phys. Rev. C **99**, 035501 (2019).

[61] A. O. Sushkov, O. P. Sushkov, and A. Yaresko, Phys. Rev. A **107**, 062823 (2023).

[62] C. Abel *et al.*, Phys. Rev. Lett. **124**, 081803 (2020).

[63] P. W. Graham and S. Rajendran, Phys. Rev. D **88**, 035023 (2013).

[64] T. S. Roussy *et al.*, Phys. Rev. Lett. **126**, 171301 (2021).

[65] D. Aybas *et al.*, Phys. Rev. Lett. **126**, 141802 (2021).

[66] E. B. Aleksandrov, Opt. Spectrosc. **14**, 232 (1963).

[67] J. Dodd, R. Kaul, and D. Warrington, Proc. Phys. Soc. **84**, 176 (1964).

[68] T. Hadeishi and W. A. Nierenberg, Phys. Rev. Lett. **14**, 891 (1965).

[69] S. Haroche, J. Paisner, and A. Schawlow, Phys. Rev. Lett. **30**, 948 (1973).

[70] E. B. Aleksandrov, N. I. Kaliteevskii, and M. Chaika, Sov. Phys. Uspekhi **22**, 760 (1979).

[71] R. Vreeker, M. Casaldoni, and M. Glasbeek, Chem. Phys. Lett. **115**, 69 (1985).

[72] E. Hack and J. Huber, Int. Rev. Phys. Chem. **10**, 287 (1991).

[73] D. Kawall, F. Bay, S. Bickman, Y. Jiang, and D. DeMille, Phys. Rev. Lett. **92**, 133007 (2004).

[74] V. S. Malinovsky and J. L. Krause, Euro. Phys. J. D **14**, 147 (2001).

[75] M. H. Montgomery and D. O'Donoghue, Delta Scuti Star Newsletter **13**, 28 (1999).

[76] A. Abragam and B. Bleaney, *Electron paramagnetic resonance of transition ions* (Oxford University Press, 2012).

[77] A. L. Alexander, J. J. Longdell, and M. J. Sellars, J. Opt. Soc. Am. B **24**, 2479 (2007).

[78] R. W. P. Drever, J. L. Hall, F. V. Kowalski, J. Hough, G. M. Ford, and H. Ward, Appl. Phys. B **2**, 97–105 (1983).

[79] E. A. Donley, T. P. Heavner, F. Levi, M. O. Tataw, and S. R. Jefferts, Rev. Sci. Instrum. **76**, 063112 (2005).

[80] M. Kim, R. Notermans, C. Overstreet, J. Curti, P. Asenbaum, and M. A. Kasevich, Opt. Lett. **45**, 6555 (2020).

[81] R. Gangradey, V. Tanna, S. Mukherjee, J. Mishra, P. Nayak, and P. Panchal, Vacuum **172**, 109026 (2020).

[82] J. Ford, *Toward a T-violation measurement in a solid-state system*, Master's thesis, University of Toronto, Toronto, Canada (2023).

[83] A. Ortu, *Rare earth quantum memories: spectroscopy of a new platform and quantum storage implementations*, Ph.D. thesis, University of Geneva, Geneva, Switzerland (2021), available at `https://archive-ouverte.unige.ch/unige:158720`.

[84] A. Ferrier, B. Tumino, and P. Goldner, J. Luminescence **170**, 406 (2016).